Received: 17 December 2021 | Revised: 6 April 2022 | Accepted: 11 April 2022

DOI: 10.1002/esp.5386

RESEARCH ARTICLE

ESPL WILEY

Temporal evolution of headwall erosion rates derived from cosmogenic nuclide concentrations in the medial moraines of Glacier d'Otemma, Switzerland

Katharina Wetterauer[1] | Dirk Scherler[1,2] | Leif S. Anderson[1,3,4] | Hella Wittmann[1]

[1]GFZ German Research Centre for Geosciences, Potsdam, Germany

[2]Institute of Geological Sciences, Freie Universität Berlin, Berlin, Germany

[3]Institute of Earth Surface Dynamics, University of Lausanne, Lausanne, Switzerland

[4]Department of Geology and Geophysics, The University of Utah, Salt Lake City, Utah, USA

Correspondence
Katharina Wetterauer, GFZ German Research Centre for Geosciences, Telegrafenberg, 14473, Potsdam, Germany.
Email: kwett@gfz-potsdam.de

Funding information
European Research Council (ERC) H2020-EU.1.1., Grant/Award Number: 759639

Abstract

Climate change affects the stability and erosion of high-alpine rock walls above glaciers (headwalls) that deliver debris to glacier surfaces. Since supraglacial debris in the ablation zone alters the melt behaviour of the underlying ice, the responses of debris-covered glaciers and of headwalls to climate change may be coupled. In this study, we analyse the beryllium-10 (^{10}Be)-cosmogenic nuclide concentration history of glacial headwalls delivering debris to the Glacier d'Otemma in Switzerland. By systematic downglacier-profile-sampling of two parallel medial moraines, we assess changes in headwall erosion through time for small, well-defined debris source areas. We compute apparent headwall erosion rates from ^{10}Be concentrations ([^{10}Be]), measured in 15 amalgamated medial moraine debris samples. To estimate both the additional ^{10}Be production during glacial debris transport and the age of our samples we combine our field-based data with a simple model that simulates downglacier debris trajectories. Furthermore, we evaluate additional grain size fractions for eight samples to test for stochastic mass wasting effects on [^{10}Be]. Our results indicate that [^{10}Be] along the medial moraines vary systematically with time and consistently for different grain sizes. [^{10}Be] are higher for older debris, closer to the glacier terminus, and lower for younger debris, closer to the glacier head. Computed apparent headwall erosion rates vary between ~0.6 and 10.8 mm yr^{-1}, increasing over a maximum time span of ~200 years towards the present. As ice cover retreats, newly exposed headwall surfaces may become susceptible to enhanced weathering and erosion, expand to lower elevations, and contribute formerly shielded bedrock of likely different [^{10}Be]. Hence, we suggest that recently lower [^{10}Be] reflect the deglaciation of the debris source areas since the end of the Little Ice Age.

KEYWORDS
cosmogenic ^{10}Be, deglaciation, headwall erosion rates, medial moraines, mountain glacier

1 | INTRODUCTION

The sensitivity of high-alpine glacial landscapes to climate change is a matter of growing concern. In the European Alps, one of the world's most populated mountainous regions (Haeberli & Beniston, 1998), rock falls and slope failures endanger communities, infrastructure and the tourist economy (e.g., Haeberli et al., 1997; Haeberli & Beniston, 1998; Hartmeyer et al., 2020a, 2020b). Previous studies suggest that enhanced rock fall activities and slope failures during the last three decades are related to permafrost degradation and/or changes in frost weathering (e.g., Gruber & Haeberli, 2007; Gruber et al., 2004; Huggel et al., 2010, 2012; Phillips et al., 2016; Ravanel &

Deline, 2009; Ravanel et al., 2010). Increased mass wasting has also been linked to glacial thinning and associated stress changes in the adjacent bedrock (e.g., Ballantyne, 2002; Cossart et al., 2008; Hartmeyer et al., 2020a, 2020b). At the same time, studies on glaciers from various mountain ranges report an increase in debris cover over decades (e.g., Bolch et al., 2008; Deline, 2005; Glasser et al., 2016; Kirkbride, 1993). This modifies ice ablation and may delay warming-induced glacier retreat and alter regional impacts (e.g., Anderson & Anderson, 2016; Benn et al., 2012; Rowan et al., 2015; Scherler et al., 2011; Vincent et al., 2016). Therefore, if climate warming induces an increase in debris delivery to glacier surfaces and a thickening of glacial debris cover, climate change-related responses of rock walls and adjacent glaciers are likely interrelated (Scherler & Egholm, 2020).

Climate variability throughout the Holocene caused glaciers to repeatedly advance and retreat in the European Alps (Holzhauser et al., 2005). Since their maximum Little Ice Age (LIA) extent, typically around 1850 (Ivy-Ochs et al., 2009), Alpine glaciers underwent widespread and pronounced decline (Zemp et al., 2008). Their retreat accounted for about ~50% of Alpine ice cover loss by 2000, despite brief re-advances in the 1890s, 1920s, 1970s and 1980s (Zemp et al., 2008, and references cited therein); and glacier retreat has accelerated since the 1980s (e.g., GLAMOS, 2019a, 2019b; Huss, 2012; Paul et al., 2004; Zemp et al., 2008, 2019). On several glaciers in the European Alps debris cover extent has substantially expanded since the end of the LIA (e.g., Deline, 2005; Fleischer et al., 2021). Observations of clean-ice glaciers transforming into debris-covered glaciers and rapid expansion of supraglacial debris (Deline, 2005) may be the result of more frequent rock falls and debris deposition on glaciers, in addition to increasing ablation areas.

Yet, temporal changes in rock wall erosion above glaciers are largely unconstrained. Estimates for the post-LIA deglaciation period are rare and mainly based on records of a few years or decades (e.g., Hartmeyer et al., 2020a, 2020b; Rabatel et al., 2008; Sass, 2005). To quantify long-term (> 10^2–10^4 years) erosion rates within glacial catchments recent studies have analysed concentrations of the *in situ*-produced cosmogenic nuclide beryllium-10 (^{10}Be) ([^{10}Be], atoms g^{-1}) in supraglacial debris (e.g., Guillon et al., 2015; Heimsath & McGlynn, 2008; Sarr et al., 2019; Seong et al., 2009). For example, Ward and Anderson (2011) measured [^{10}Be] in supraglacial debris samples collected along medial moraines on Alaskan glaciers to estimate spatially- and temporally-averaged erosion rates for distinct headwalls. This strategy was revisited by Scherler and Egholm (2020), who combined field-based data with a numerical ice flow model to track [^{10}Be] along a medial moraine of the Chhota Shigri Glacier in the Himalaya and to evaluate temporal variations in headwall erosion rates.

However, these previous studies employed a rather widely-spaced or limited sampling scheme and little is known about the processes governing variations in [^{10}Be] along medial moraines. Specifically, low-frequency high-magnitude mass wasting processes, such as landslides and debris flows, can impact detrital cosmogenic nuclide concentrations, often manifesting themselves in grain size-dependent nuclide concentrations (e.g., Kober et al., 2012; Niemi et al., 2005; Puchol et al., 2014; West et al., 2014). Using a non-representative grain size fraction, therefore, could bias the quantification of long-term erosion rates.

In this study we quantify headwall erosion rates (i.e., the process of headwall retreat perpendicular to the bedrock surface) from medial moraine debris of a glacier in the European Alps and assess changes thereof through time in a systematic way. For our analysis, we chose Glacier d'Otemma in Switzerland, where the availability of long-term monitoring data sets and historical documents allows for greater in-depth analysis than at glaciers in more remote regions. We sampled two parallel medial moraines that have small and well-defined source areas. Samples were taken at regular intervals and at high spatial density to test for systematic downglacier variations in [^{10}Be]. In addition, we analyse different grain size fractions to identify the potential role of stochastic mass wasting events. We combine our field-based data with a simple model that simulates debris trajectories through the glacier, allowing us to estimate both the additional production of cosmogenic nuclides during glacial transport and the age of our samples.

2 | GLACIAL HEADWALLS AND MEDIAL MORAINES

Steep ice-free rock walls are prominent landforms in glacial landscapes. Where they tower at the head of valley glaciers, they are often called glacial headwalls. Being exposed to weathering and erosion, these headwalls retreat and shed bedrock debris onto the ice surface that is eventually transported away from the source by the moving ice. The debris entrainment itself varies with its deposition relative to the equilibrium line altitude (ELA, the elevation where annual ice accumulation balances ablation). In the glacier's accumulation zone above the ELA, debris delivered from headwalls is buried by the accumulating ice. It is first transported downglacier within the ice ('englacial'), before it subsequently re-emerges at the surface below the ELA, and continues to be transported on the ice surface ('supraglacial'). In the glacier's ablation zone below the ELA, debris remains on the ice surface, unless it falls into crevasses or off the glacier (e.g., see summaries in Kirkbride, 1995; Benn & Evans, 1998; Ward & Anderson, 2011).

Medial moraines are the surficial expression of ice-flow parallel debris bands in a glacier's ablation zone. They form where debris that has been deposited in the accumulation zone and entrained englacially is melting out below the ELA, or where two neighbouring glaciers join below the ELA and their supraglacial marginal debris (lateral moraines) merges (e.g., Anderson, 2000; Boulton & Eyles, 1979; Eyles & Rogerson, 1978a, 1978b; Gomez & Small, 1985). Following the laminar flow of ice, this debris is passively transported downglacier and as a result, medial moraine debris deposits tend to be older downglacier. Supraglacial debris has a strong control on melt rates. As shown by Østrem (1959) and numerous subsequent studies (e.g., Anderson & Anderson, 2016; Mattson et al., 1993; Nicholson & Benn, 2006; Reid & Brock, 2010), sub-debris melt rates below a debris cover thinner than a certain 'critical thickness' (often around 2 cm) are higher than clean-ice melt rates but will be reduced underneath a thicker debris cover. Accordingly, the insulating effect of supraglacial debris exponentially reduces sub-debris melt rates as debris cover thickness increases. Therefore, medial moraines often form ridges on the glacier surface because the adjacent bare ice melts faster (e.g., Anderson, 2000; Boulton & Eyles, 1979; Eyles & Rogerson, 1978a, 1978b; Gomez & Small, 1985). For these reasons, medial moraines

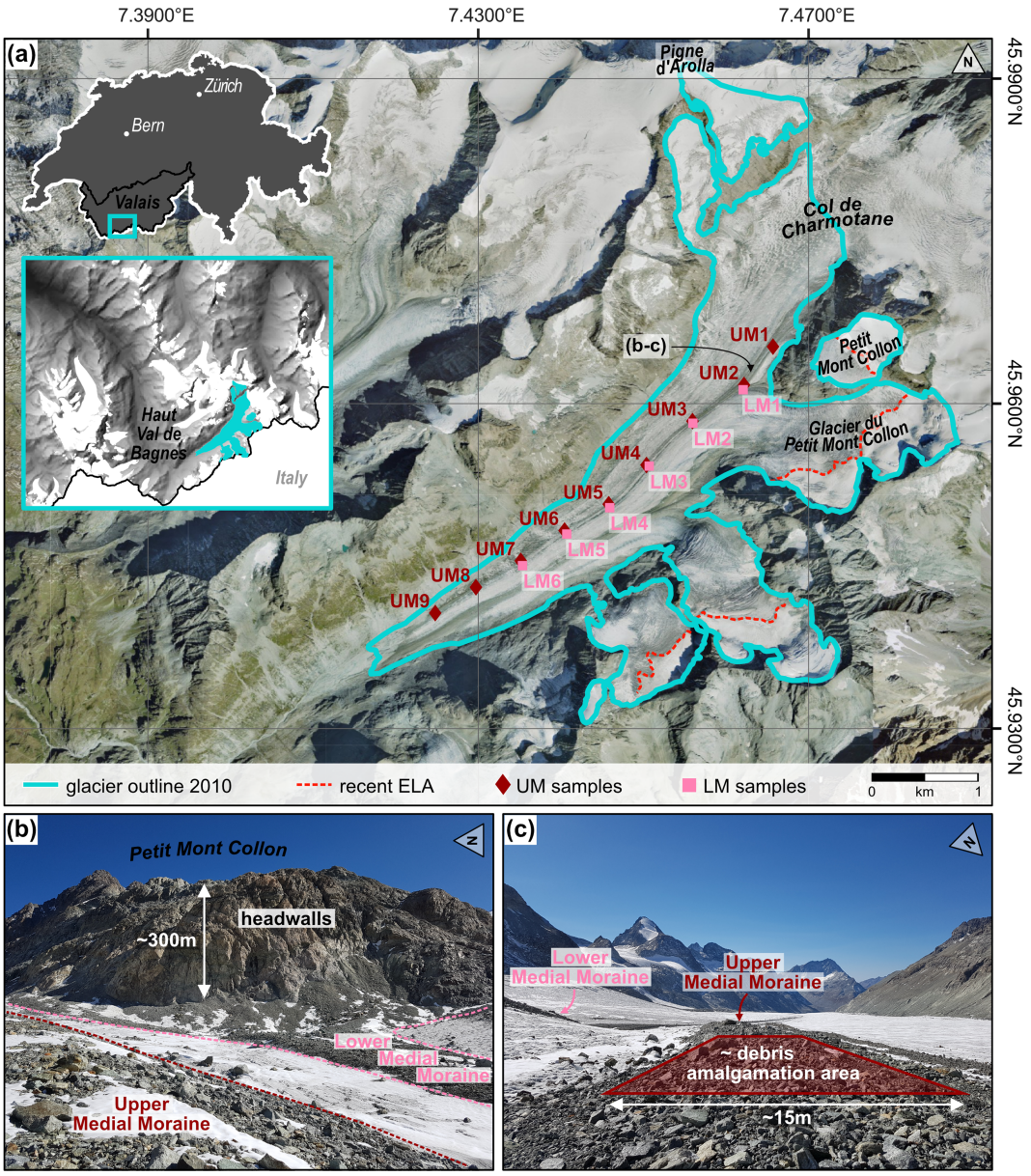

FIGURE 1 Glacier d'Otemma, Switzerland. (a) Orthoimage showing the glacier with its catchment, the debris source area Petit Mont Collon, the UM and LM sample locations, and the approximate recent ELA. The upper inset outlines the location of the glaciated Haut Val de Bagnes in Switzerland, the lower inset zooms on the glacier's location in the Haut Val de Bagnes (orthoimage from 2017 by swisstopo, 2021; glacier outline by Fischer et al., 2014). (b) Field photograph of the headwalls that contribute debris to the LM. (c) Field photograph of the UM downglacier pathway with indicated concept of supraglacial sample amalgamation. Note that UM and LM are separated by an ice septum (photographs taken in October 2018 from an UM position as indicated in (a)). UM/LM, upper/lower medial moraine; ELA, equilibrium line altitude [Color figure can be viewed at wileyonlinelibrary.com]

may serve as useful and visibly traceable archives to study headwall erosion histories.

3 | STUDY AREA

3.1 | Glacier d'Otemma and its catchment

Glacier d'Otemma is a Swiss valley glacier located in the southern part of the Valais, close to the Swiss-Italian border (Figure 1a). Originating at the southern flank of the Pigne d'Arolla and fed by several smaller tributary glaciers, the main glacier flows southwest into the Haut Val de Bagnes. At present, Glacier d'Otemma has a length of ~6 km and is likely entirely composed of temperate ice (Langhammer et al., 2017). The main trunk ranges from ~3015 m elevation at the ice divide at the Col de Charmotane, down to ~2500 m elevation at its terminus (elevations in this article are stated as above mean sea level). Its maximum ice thickness was estimated to be ~290 m close to the ice divide in the year 2009 (Gabbi et al., 2012), and the ice-covered area was ~15.5 km^2 in the year 2013 (GLAMOS, 2019b). From high resolution satellite images of the glacier catchment from the year 2017, we estimate that at present, the ELA is located above ~3100 m elevation.

Systematic long-term monitoring of glacier changes in the Swiss Alps (Glacier Monitoring Switzerland; GLAMOS, 2019a, 2019b, 2021) as well as historical maps, orthoimages, and photographs (Federal Office of Topography swisstopo; swisstopo, 2021) reveal a continuous recession history of Glacier d'Otemma since the end of the 19th century (Mancini & Lane, 2020), unlike many other Alpine glaciers

(Zemp et al., 2008, and references cited therein). The terminus retreated about 2.3 km between 1881 and 2016 (GLAMOS, 2019a). Between 1850 and 2010 the glacier lost ~40% of its surface area and ~60% of its ice volume, while glacier thinning reached ~70 m at the ice divide (Lambiel & Talon, 2019). The geodetic glacier-wide mass balance decreased from approximately −0.4 m water equivalent (w.e.) yr^{-1} between 1934 and 1983 to approximately −1.0 m w.e. yr^{-1} between 1983 and 2013 (GLAMOS, 2019b). Thus, Glacier d'Otemma has been losing mass faster than the average glacier in the Swiss Alps (−0.62 m w.e. yr^{-1} between 1980 and 2010), implying a high sensitivity to climate change (Fischer et al., 2015). Gabbi et al. (2012), who modelled the future evolution of several glaciers in the Haut Val de Bagnes, predict that Glacier d'Otemma will retreat even faster in the future, reducing to some relict ice patches by 2070.

3.2 | Medial moraines and their source areas

A major bedrock source delivering debris to Glacier d'Otemma is the Petit Mont Collon, a nunatak with a peak at ~3555 m elevation (Figure 1a,b). Its west-northwest facing and south-southwest facing headwalls are flanked by the glacier's main trunk and the small tributary Glacier du Petit Mont Collon, respectively. These headwalls are located in the distribution zone of modelled mountain permafrost in the Swiss Alps (BAFU, 2005). They tower up to ~500 m above the glacier surface, with slopes up to ~60°. While the steeper faces are largely ice-free bedrock, the saddle-like centre of Petit Mont Collon is covered by remnants of a small glacier (Figure 2). In 1973, this isolated glacier used to flow into Glacier d'Otemma and, before, in 1850, its accumulation zone was connected to Glacier d'Otemma (swisstopo, 2021). Petit Mont Collon is composed mainly of gneiss and schist (Figure 2). Only the northernmost and highest flanks are composed of gabbro (swisstopo, 2021).

Two pronounced medial moraines are nourished from Petit Mont Collon (Figures 1a and 2). They are fed by different but adjacent rock faces and from now on we refer to them as the upper medial moraine (UM) and lower medial moraine (LM). Debris input from higher up is prevented by the isolated nature of Petit Mont Collon at the ice divide. Running parallel and mostly 20–40 m apart from each other, UM and LM exist between 3000 and 2650 m elevation. Currently, the UM originates slightly above the 3000 m elevation contour, off the west-northwest facing headwalls and is clearly traceable > 4 km distance downglacier. The LM starts slightly below 3000 m elevation, off the south-southwest facing headwalls near the recent ice confluence, and is well traceable along a downglacier distance of ~3 km. Close to their source areas (Figure 1b,c), both moraines have widths of up to ~20 m and a relief of ~3 m, but they narrow down to ~6 m and flatten out in the central part of the glacier. At present, debris deposition and transport in the UM and LM occur entirely in the glacier's ablation zone (Figures 1 and 2), implying that, except for seasonal snow cover, the debris currently falling on the glacier is permanently exposed.

4 | MATERIAL AND METHODS

We provide an accompanying data publication with this study, which comprises the cosmogenic nuclide data and detailed descriptions of the sample processing and setup of our model, including its evaluation (Wetterauer et al., 2022). Figures and sections in the data publication are here referred to as Figures S1–S7 and Sections S1–S6.

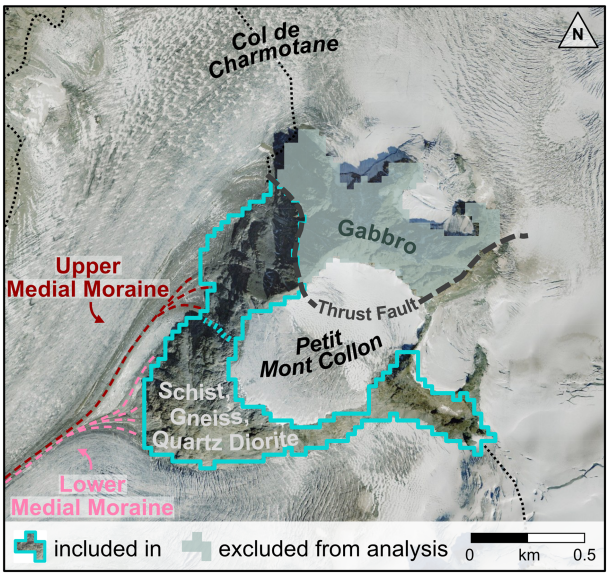

FIGURE 2 Debris source area Petit Mont Collon and simplified bedrock lithology of the headwalls. We only consider headwalls which are made of schist, gneiss or quartz diorite and which deposit debris below the ice divide at the Col de Charmotane. The source headwalls are separated from gabbroic areas by a mapped thrust fault (dashed grey line) and differentiated into headwalls to the upper or lower medial moraine (dashed cyan line). Note that the angular course of the headwall outline is the result of superimposing the glacier's 2010 outline onto a 30 m resolution DEM. The glacier's 2010 outline (black dotted line) and the pathways of the upper/lower medial moraine (dashed red/pink lines) are indicated (orthoimage from 2017 and lithologic mapping by swisstopo, 2021; glacier outline by Fischer et al., 2014) [Color figure can be viewed at wileyonlinelibrary.com]

4.1 | Medial moraine samples

In October 2018 we collected 15 debris samples from the UM and LM (Table 1 and Figure 1a). Samples (~7 kg each) were collected downglacier every ~500 m. Nine samples were taken from the UM (UM1–UM9) along a ~4.2 km long profile, between 2918 and 2547 m elevation. Six samples were taken from the LM (LM1–LM6) along a ~2.7 km long profile, between 2875 and 2668 m elevation. Samples were mainly composed of schist and gneiss clasts with grain sizes ranging from coarse sand (~1 mm) to pebble (~30 mm) size (Figure S1). Clasts were randomly collected (amalgamated) over the moraine surface (Figure 1c). The collection area for each sample was approximately 10 m × 30 m near the debris source areas and the glacier terminus, and approximately 6 m × 20 m in the central glacier region where the medial moraines are narrower. Over the sampled distance, the moraine topography was relatively smooth and not intersected by open crevasses. We found no obvious indicators for lateral debris input, such as runout deposits from valley side walls traversing onto the ice, or for basal debris input, such as aligned deposits sheared onto the glacier surface by internal ice thrusting or rounded clasts (e.g., Alley et al., 1997; Boulton, 1978).

TABLE 1 Data for medial moraine debris samples collected on Glacier d'Otemma

Sample[a]	Latitude (°N)	Longitude (°E)	Elevation (m)	Downglacier distance[b] (m)	Performed analysis[c] /f	/c	GS
Upper medial moraine (UM)							
UM1	45.9653	7.4657	2918	0	X	X	
UM2	45.9617	7.4622	2882	478	X		X
UM3	45.9584	7.4559	2837	1088	X	X	
UM4	45.9543	7.4504	2789	1712	X	X	
UM5	45.9507	7.4458	2747	2248	X	X	
UM6	45.9483	7.4405	2707	2743	X		
UM7	45.9455	7.4352	2663	3258	X	X	
UM8	45.9431	7.4297	2600	3758	X		
UM9	45.9407	7.4248	2547	4224	X	X	
Lower medial moraine (LM)							
LM1	45.9613	7.4621	2875	0	X		X
LM2	45.9582	7.4560	2835	581	X		
LM3	45.9542	7.4507	2791	1184	X		
LM4	45.9504	7.4459	2749	1745	X		
LM5	45.9480	7.4407	2712	2228	X		
LM6	45.9450	7.4354	2668	2754	X		

[a]Amalgamated supraglacial debris samples.
[b]Distance from uppermost sample UM1 and LM1 of upper and lower medial moraine, respectively.
[c]/f = fine-grained fraction (0.125–4 mm), /c = coarse-grained fraction (4–22.4 mm), GS = grain size sub-samples (0.125–0.8, 0.8–2, 2–4, 4–8 and 8–16 mm).

Cosmogenic nuclide sample processing was performed according to standard *in situ*-produced ^{10}Be separation techniques (e.g., von Blanckenburg et al., 2004). Debris samples were sieved into different fractions (Figure S1) and processed at the Helmholtz Laboratory for the Geochemistry of the Earth Surface (HELGES) at the GFZ German Research Centre for Geosciences in Potsdam, Germany. A total of 29 ^{10}Be/^{9}Be ratio measurements (Table 2) were carried out using accelerator mass spectrometry (AMS) at the University of Cologne, Germany (Dewald et al., 2013), and normalized to the standards KN01-6-2 (nominal ^{10}Be/^{9}Be value: 5.35×10^{-13}) and KN01-5-3 (nominal ^{10}Be/^{9}Be value: 6.32×10^{-12}). Details are provided in Wetterauer et al. (2022).

To ensure comparability, we primarily focused on a fine grain size fraction of 0.125–4 mm for all samples. To explore potential grain size effects, we additionally analysed a coarser grain size fraction of 4–22.4 mm from almost every second sample on the UM. At higher resolution, we separately analysed the five grain size fractions 0.125–0.8, 0.8–2, 2–4, 4–8, and 8–16 mm for the samples UM2 and LM1 (Tables 1 and 2).

4.2 | Cosmogenic nuclides in medial moraine debris

Quantifying headwall erosion rates from [^{10}Be] in supraglacial debris relies on knowledge of (i) the ^{10}Be production rate in the headwall, which allows to quantify [^{10}Be] in the headwall ('$[^{10}Be]_{headwall}$'), and (ii) the ^{10}Be production rate during downglacier debris transport, which allows to quantify [^{10}Be] accumulated during glacial transport ('$[^{10}Be]_{transport}$'). The sum of these two components is the measured [^{10}Be] in supraglacial debris samples ('$[^{10}Be]_{measured}$'). To disentangle them, we developed a simple one-dimensional (1D) model to predict $[^{10}Be]_{transport}$ by estimating debris transport trajectories for our samples (see Section 4.3). We then subtract $[^{10}Be]_{transport}$ from $[^{10}Be]_{measured}$ in order to estimate $[^{10}Be]_{headwall}$.

Using the estimated $[^{10}Be]_{headwall}$, Equation 1 (Lal, 1991) allows us to determine 'apparent' headwall erosion rates E (mm yr^{-1}):

$$\left[{}^{10}\mathrm{Be}\right]_{\mathrm{headwall}}(z) = \frac{P_{\mathrm{sp}}(0)}{\lambda + \frac{\rho E}{\Lambda}} e^{-z\left(\frac{\rho}{\Lambda}\right)} \quad (1)$$

When assuming a steadily eroding bedrock surface and an initial bedrock concentration of zero, $[^{10}Be]_{headwall}(z)$ is the ^{10}Be concentration (atoms g^{-1}) in the headwall as a function of bedrock depth z (cm), $P_{sp}(0)$ is the spallogenic surface production rate (atoms g^{-1} yr^{-1}), λ is the decay constant (yr^{-1}) (based on a half-life of 1.387 ± 0.012 Myr; Chmeleff et al., 2010; Korschinek et al., 2010), ρ is the material density (g cm^{-3}), and Λ is the absorption mean free path (g cm^{-2}). Building on the steady-state assumption, but being aware that headwalls may inherit nuclide signatures from alternating episodes of exposure and coverage as well as from changing erosion rates during these phases, we consider our rates to be 'apparent' headwall erosion rates.

We computed ^{10}Be production rates for ice-free surfaces using a digital elevation model (DEM) of 30 m resolution (global raster dataset SRTM GL1; NASA Shuttle Radar Topography Mission SRTM, 2013) using MATLAB® and TopoToolbox Version 2 (Schwanghart & Scherler, 2014). Gabbroic headwall areas were excluded due to their low quartz content (Figure 2). We determined mean headwall ^{10}Be

TABLE 2 Measured accelerator mass spectrometry (AMS) $^{10}Be/^{9}Be$ ratios and ^{10}Be concentrations

Sample	Grain size (mm)	Qtz mass (g)	Carrier mass (mg)	AMS $^{10}Be/^{9}Be$ $\times 10^{-14}$ $\pm$ 1σ	$[^{10}Be]_{measured}$ $\times 10^{3}$ (atoms g^{-1}) $\pm$ 1σ	Blank[a]
Upper medial moraine (UM)						
Fine-grained samples						
UM1/f	0.125–4	26.78	0.200	1.47 ± 0.15	5.53 ± 0.57	B3
UM2/f[b]	0.125–4	–	–	–	7.41 ± 0.79	–
UM3/f	0.125–4	26.88	0.200	1.73 ± 0.15	6.52 ± 0.57	B3
UM4/f	0.125–4	22.82	0.201	8.50 ± 0.40	38.32 ± 1.86	B3
UM5/f	0.125–4	23.06	0.201	2.47 ± 0.17	10.96 ± 0.78	B3
UM6/f	0.125–4	22.97	0.200	3.48 ± 0.22	15.52 ± 0.98	B3
UM7/f	0.125–4	23.39	0.200	6.19 ± 0.39	26.34 ± 1.74	B2
UM8/f	0.125–4	22.39	0.201	4.43 ± 0.26	20.32 ± 1.23	B3
UM9/f	0.125–4	22.67	0.200	4.12 ± 0.25	18.59 ± 1.14	B3
Coarse-grained samples						
UM1/c	4–22.4	32.25	0.200	1.23 ± 0.15	3.69 ± 0.47	B4
UM3/c	4–22.4	32.69	0.200	1.03 ± 0.12	3.01 ± 0.38	B4
UM4/c	4–22.4	37.09	0.205	1.65 ± 0.15	4.48 ± 0.44	B5
UM5/c	4–22.4	25.07	0.200	1.89 ± 0.18	7.47 ± 0.76	B4
UM7/c	4–22.4	32.43	0.200	4.19 ± 0.28	13.06 ± 0.89	B4
UM9/c	4–22.4	32.69	0.200	5.48 ± 0.31	17.03 ± 1.00	B4
Grain size sub-samples						
UM2/0.8	0.125–0.8	21.29	0.206	2.30 ± 0.22	9.34 ± 1.18	B1
UM2/2	0.8–2	23.47	0.199	2.12 ± 0.18	8.30 ± 0.82	B2
UM2/4	2–4	32.07	0.200	1.78 ± 0.16	5.47 ± 0.51	B4
UM2/8	4–8	32.12	0.199	3.12 ± 0.21	9.70 ± 0.69	B4
UM2/16	8–16	32.78	0.200	0.65 ± 0.11	1.80 ± 0.34	B4
Lower medial moraine (LM)						
Fine-grained samples						
LM1/f[b]	0.125–4	–	–	–––	17.78 ± 1.14	–
LM2/f	0.125–4	22.64	0.200	4.94 ± 0.30	22.37 ± 1.39	B3
LM3/f	0.125–4	14.54	0.200	2.07 ± 0.18	13.09 ± 1.32	B2
LM4/f	0.125–4	20.31	0.199	2.72 ± 0.21	12.66 ± 1.10	B2
LM5/f	0.125–4	22.90	0.201	3.28 ± 0.22	14.68 ± 0.99	B3
LM6/f	0.125–4	17.11	0.200	5.34 ± 0.32	30.81 ± 2.00	B2
Grain size sub-samples						
LM1/0.8	0.125–0.8	26.98	0.206	4.31 ± 0.31	15.27 ± 1.26	B1
LM1/2	0.8–2	22.58	0.201	3.58 ± 0.23	16.28 ± 1.06	B3
LM1/4	2–4	31.87	0.200	6.56 ± 0.33	20.97 ± 1.10	B4
LM1/8	4–8	32.08	0.200	5.75 ± 0.33	18.22 ± 1.08	B4
LM1/16	8–16	21.51	0.201	2.83 ± 0.23	13.23 ± 1.14	B4

[a]Process blank used to correct respective sample batches, where corresponding $^{10}Be/^{9}Be$ ratios are B1 = 4.43×10^{-15}, B2 = 2.16×10^{-15}, B3 = 2.55×10^{-16}, B4 = 7.65×10^{-16}, B5 = 1.19×10^{-15}.
[b]$[^{10}Be]$ calculated from corresponding weighted mean of separate measurements of fractions 0.125–0.8, 0.8–2 and 2–4 mm.

production rates for three different time slices using reconstructed glacier outlines (Figure 3) that document the ice extent of Glacier d'Otemma for the years 2010 (approximate recent ice extent; Fischer et al., 2014), 1973 (interim stage; Müller et al., 1976), and 1850 (approximate final LIA extent; Maisch et al., 2000). We refined the 1850 glacier outline in the headwall region using the first editions of the Dufour and Siegfried Map (swisstopo, 2021) as well as the 1850 LIA ice extent in the Haut Val de Bagnes as reconstructed by Lambiel and Talon (2019). To examine both moraines individually, we subdivided the debris source area into UM headwalls and LM headwalls (Figures 2 and 3b–d), using the DEM and the flow directions following the steepest decent approach.

All ^{10}Be production rates were calculated with the functions provided by the CRONUS online calculator version 2.3

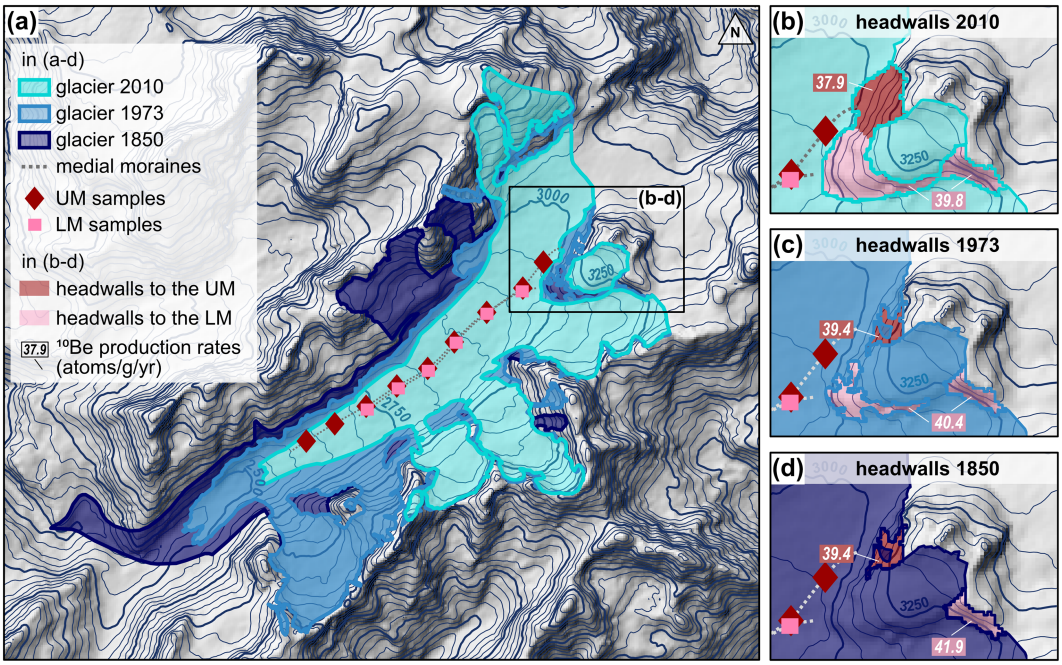

FIGURE 3 Glacier d'Otemma and debris source area Petit Mont Collon in 2010, 1973 and 1850 (glacier outlines by Fischer et al., 2014, and Müller et al., 1976, and modified from Maisch et al., 2000). (a) Contour grid depicting the three superimposed glacier extents. (b–d) Detail of the ice-covered and ice-free areas of the source headwalls and computed average ^{10}Be production rates in (b) 2010 (c) 1973 and (d) 1850. The contour line spacing corresponds to 50 m elevation and is based on the recent DEM where the glacier extent is smallest. Therefore, contour lines on the glacier body itself are only valid for the most recent glacier extent in 2010. UM/LM, upper/lower medial moraine [Color figure can be viewed at wileyonlinelibrary.com]

(Balco et al., 2008), using the constant spallation scaling scheme 'St' (Lal, 1991; Stone, 2000) and a sea level high latitude spallation production rate of 4.01 ± 0.33 atoms g^{-1} yr^{-1} (Borchers et al., 2016). We neglected temporal variations in production rates due to paleomagnetic intensity changes as most of our samples are likely younger than ~200 years (see Section 5.2). Moreover, we neglected production by muons in the headwalls as it accounts for < 1% of the spallogenic production near the bedrock surface. Effects of topographic shielding on nuclide production rates were estimated following Dunne et al. (1999) as implemented in the TopoToolbox Version 2 (Schwanghart & Scherler, 2014). Snow cover shielding of the headwalls was neglected as large bedrock areas seem to remain snow-free during snow cover seasons (swisstopo, 2021). We assumed a bedrock density ρ_r of 2.65 g cm^{-3} in Equation 1 and also considered the surface slope dependency of cosmic ray attenuation in bedrock by calculating the absorption mean free path Λ for each DEM pixel following Masarik et al. (2000). Since headwall erosion rates are measured perpendicular to the surface, we applied an area correction using the local slope angle to compute mean production rates.

4.3 | Computation of downglacier debris transport

The $[^{10}Be]_{transport}$ is small compared to $[^{10}Be]_{headwall}$ in settings where erosion rates are low, glacier transport pathways are short or mainly englacial, glacier surface velocities are high (≥ 30 m yr^{-1}), and environmental conditions are constant (Scherler & Egholm, 2020; Ward & Anderson, 2011). However, $[^{10}Be]_{transport}$ may be substantial if erosion rates are very high, if transport is far and/or slow, and predominantly supraglacial. Since both glacier velocity and transport depth vary downglacier and through time when the glacier is changing, the relative contribution of $[^{10}Be]_{transport}$ to $[^{10}Be]_{measured}$ must vary in time, too.

To estimate both $[^{10}Be]_{transport}$ and the ages of our samples, we developed a simple 1D model to reconstruct time-depth pathways (Figure 4). We first derived modern horizontal glacier surface velocities by cross-correlating satellite imagery (Figure S2c; Leprince et al., 2007; Scherler et al., 2008), and by tracking boulders on historical aerial images (Figure S2c; swisstopo, 2021). We then calibrated a simple model using the centre-line velocity profile and recent ice thickness and surface slope estimates, by tuning the rate parameter in Glen's flow law (Figure S2a–c; Glen, 1952, 1955; Farinotti et al., 2019). Using the model calibrated to present conditions, we then estimated past surface velocities with glacier thicknesses and surface slopes reconstructed for the year 1850 as input (Figures S2a–c and S3; Lambiel & Talon, 2019). To assess temporal changes in horizontal velocities, we interpolated between the ice thicknesses and slopes from 1850 and the sampling year 2018 in a three-step linear mode (Figure S2d,e). To differentiate between englacial and supraglacial transport, and to estimate debris particle burial depth, we also calculated the vertical velocity in the ice. We used a vertical mass balance profile based on a compilation of glacier mass balances from the European Alps (Figure S5; Dyurgerov, 2002). Temporal changes in vertical velocities were estimated by shifting the mass balance profile according to a reconstructed ELA history (Figure S4; Braithwaite, 2015; Kurowski, 1891). Finally, we generated particle trajectories through the glacier for all samples, computed sample ages, and estimated $[^{10}Be]_{transport}$ under consideration of seasonal snow cover (Figures S6 and S7). Details are provided in Wetterauer et al. (2022).

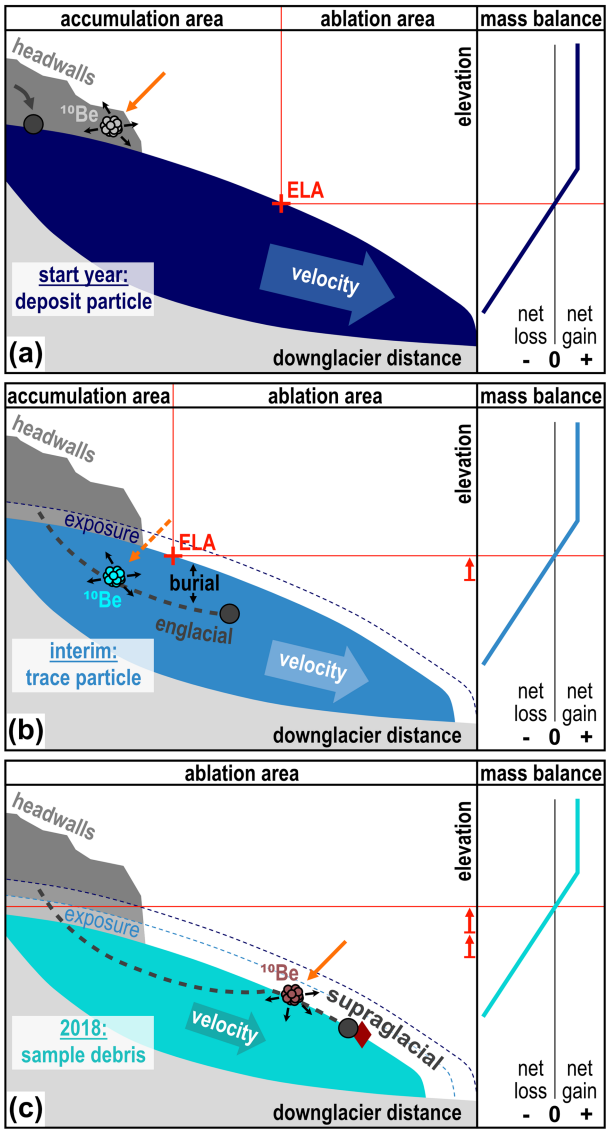

FIGURE 4 Schematic of the headwall-glacier-system and setup of the debris trajectory model. An exemplary transport scenario illustrates a debris trajectory from headwall to sample location. (a) Initially, a debris particle with the ^{10}Be signature of the headwall ($[^{10}Be]_{headwall}$) is deposited on the ice surface. (b) In the accumulation area the debris particle is buried within the ice and transported englacially. During its transport it accumulates additional ^{10}Be ($[^{10}Be]_{transport}$). (c) In the ablation area the debris particle re-emerges and is transported supraglacially until it reaches a sample's 2018 location. It inherits a combined ^{10}Be signature ($[^{10}Be]_{measured}$). Note the indication of former ice surface elevations (thin dashed lines), new bedrock exposure (highlighted stripes), decreasing glacier velocity (thinning arrows), and ELA rise and shift in mass balance (red arrows) through time. This scenario applies for our older samples (e.g., UM4–UM9). Younger samples (e.g., UM1, UM2) were deposited in the ablation area and experienced only supraglacial transport. UM/LM, upper/lower medial moraine; ELA, equilibrium line altitude [Color figure can be viewed at wileyonlinelibrary.com]

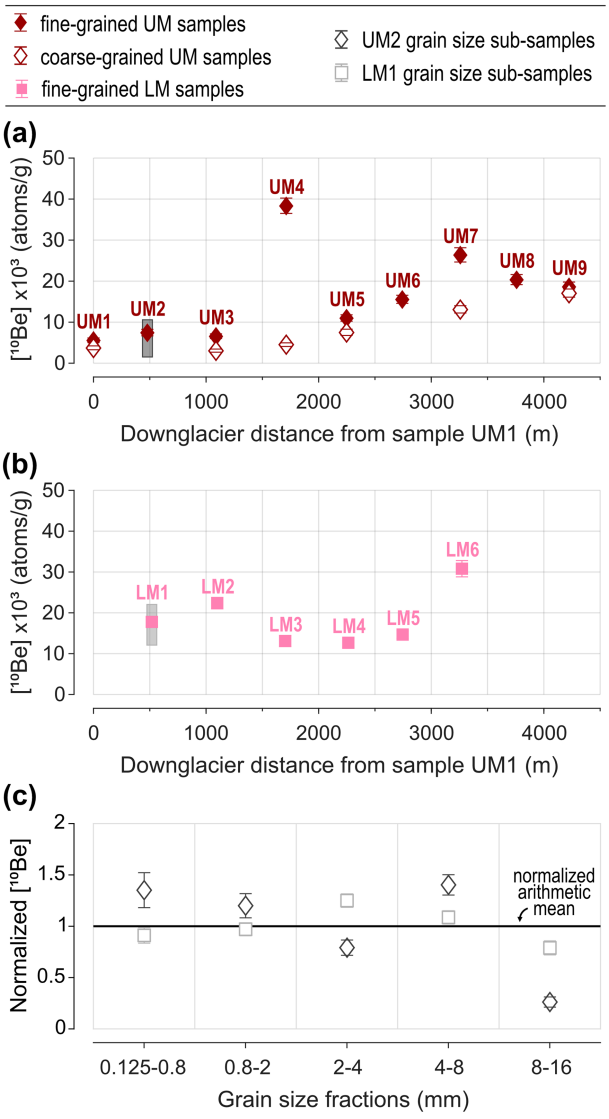

FIGURE 5 $[^{10}Be]_{measured}$ ($\pm 1\sigma$ analytical error) in medial moraine samples along Glacier d'Otemma. (a) UM [^{10}Be] obtained on a fine grain size fraction (0.125–4 mm) for all nine samples and on a coarse grain size fraction (4–22.4 mm) for every second sample. The grey bar indicates the concentration range of the grain size sub-samples from UM2. (b) LM [^{10}Be] obtained on a fine grain size fraction (0.125–4 mm) for all six samples. The grey bar indicates the concentration range of the grain size sub-samples from LM1. (c) Normalized [^{10}Be] of grain size sub-samples from UM2 and LM1. The normalization is based on the arithmetic mean of the five grain size fractions of UM2 and LM1, respectively. Note that symbol sizes are mostly larger than the analytical error and that downglacier distances were measured relative to the uppermost collected sample UM1. UM/LM, upper/lower medial moraine [Color figure can be viewed at wileyonlinelibrary.com]

5 | RESULTS

5.1 | Measured ^{10}Be concentrations

The $[^{10}Be]_{measured}$ of our 29 analysed debris sample fractions range between 2×10^3 and 38×10^3 atoms g^{-1} (Table 2 and Figure 5a,b). For the nine fine-grained (0.125–4 mm) UM samples, $[^{10}Be]_{measured}$ range between 6×10^3 and 38×10^3 atoms g^{-1} (Figure 5a). Overall, samples near the glacier head (younger deposits) have lower concentrations, whereas samples farther downglacier (older deposits) have higher concentrations. Sample UM4/f stands out with an extraordinary high concentration compared to the neighbouring samples. For the six coarse-grained (4–22.4 mm) UM samples, $[^{10}Be]_{measured}$ range between 3×10^3 and 17×10^3 atoms g^{-1}, and are thus systematically lower relative to the fine fraction, half of them differing by < 35% (Figure 5a). Only sample UM4/c differs by almost 90%. For the six fine-grained (0.125–4 mm) LM samples, $[^{10}Be]_{measured}$ vary

between 13×10^3 and 31×10^3 atoms g^{-1} (Figure 5b). Compared to the UM, LM concentrations are higher and less variable.

For our grain size sub-samples (0.125–0.8, 0.8–2, 2–4, 4–8, and 8–16 mm) from UM2 and LM1, $[^{10}Be]_{measured}$ vary between 2×10^3 and 10×10^3 atoms g^{-1} and between 13×10^3 and 21×10^3 atoms g^{-1}, respectively (indicated as grey bars in Figure 5a,b). Notably, variations in $[^{10}Be]_{measured}$ between these grain size fractions are of similar magnitude as variations between fine-grained samples along the first ~2500 and ~3000 m distance downglacier of UM and LM, respectively. To compare grain size-related variations in $[^{10}Be]_{measured}$ between the two samples (UM2 and LM1), we normalized the concentrations of each grain size fraction by the arithmetic mean of all concentrations of the respective sample (Figure 5c). In both cases, the variations are mostly < 50% and no systematic trend is discernible, although the lowest concentrations are found for the coarsest (8–16 mm) grain size sub-sample.

5.2 | Transport and headwall ^{10}Be concentrations, and sample ages

Based on our reconstructed debris trajectories (Figure S7), we estimated the age of each sample, which corresponds to the estimated debris transport time from the headwall to the sample location, and the total amount of $[^{10}Be]_{transport}$. We then derived the $[^{10}Be]_{headwall}$ by correcting $[^{10}Be]_{measured}$ for transport (Table 3 and Figure 6a). On the UM, low-concentration samples (UM1–UM3) yield ages of ~45 to 100 years, whereas high-concentration samples (UM6–UM9) yield ages of ~170 to 210 years. On the LM, the estimated transport time is shorter, with ages ranging from ~35 to 150 years. Modelled $[^{10}Be]_{transport}$ vary between $\sim 1 \times 10^3$ and 3×10^3 atoms g^{-1}. For the majority of fine-grained UM and LM samples, this accounts for less than ~25% of our $[^{10}Be]_{measured}$ (Table 3). Overall, subtracting the minor $[^{10}Be]_{transport}$ from the dominating $[^{10}Be]_{measured}$ does not change downglacier patterns for $[^{10}Be]_{headwall}$ (see Section 5.1; Figures 5a,b and 6a).

We note that for two coarser sample fractions, UM3/c and UM2/16, transport correction yielded very low and even slightly negative $[^{10}Be]_{headwall}$ values, respectively (Table 3). Especially negative concentrations are not possible, suggesting that our modelled $[^{10}Be]_{transport}$ are too high. Uncertainties in our model (see Section S4.2.5) affect particularly samples in which $[^{10}Be]_{measured}$ are comparatively low and transport is almost exclusively supraglacial, as in case of these two samples. Since our reconstructions are based on several assumptions (see Section S4.2.1) it is difficult to verify the model setup or to provide meaningful error estimates. Therefore, we do not calculate apparent headwall erosion rates for UM3/c and UM2/16. Nonetheless, given the continuous retreat history of Glacier d'Otemma (see Section 3.1), we consider it unlikely that our model-based estimates are far off the true values, especially for samples older than ~120 years that were most likely quickly buried under snow and ice (Table 3).

5.3 | Apparent headwall erosion rates

The derived apparent headwall erosion rates are reported in Table 3; for brevity, these are termed 'erosion rates' from now on. They were calculated with mean ^{10}Be production rates for UM and LM headwalls, respectively (Table 4). Overall, derived erosion rates range between 0.6 ± 0.1 and 10.8 ± 2.6 mm yr^{-1} (Figure 6b). For the fine-grained UM samples, erosion rates range between 0.6 ± 0.1 and 5.8 ± 1.0 mm yr^{-1}. Younger samples (UM1/f–UM3/f) yield higher erosion rates of 4.2 ± 0.7 to 5.8 ± 1.0 mm yr^{-1}, whereas erosion rates for older samples (UM6/f–UM9/f) are lower, spanning between 0.9 ± 0.1 and 1.6 ± 0.2 mm yr^{-1}. Erosion rates for the coarse-grained UM samples decrease from 10.8 ± 2.6 to 1.5 ± 0.2 mm yr^{-1} downglacier and with increasing age. For the fine-grained LM samples, erosion rates span a narrower range from 0.8 ± 0.1 to 2.4 ± 0.3 mm yr^{-1}. Among our grain size sub-samples from UM2 and LM1, erosion rates are fairly similar.

6 | DISCUSSION

6.1 | Grain size-dependent ^{10}Be concentrations

Grain size effects in $[^{10}Be]$ have been observed ever since the first studies have used cosmogenic nuclides for quantifying catchment-average erosion rates (e.g., Brown et al., 1995). In studies of alluvial sediments, coarser sand fractions have frequently lower cosmogenic nuclide concentrations. Such trends are typically related to slope failures and mass wasting events that excavate larger rocks with lower concentration from greater depth (e.g., Aguilar et al., 2014; Belmont et al., 2007; Brown et al., 1995, 1998; Puchol et al., 2014; Tofelde et al., 2018; van Dongen et al., 2019; West et al., 2014). Other explanations attribute grain size dependent nuclide concentrations to differences in source area properties, or to selective and abrasive fluvial transport processes (e.g., Carretier et al., 2009; Lukens et al., 2016; Matmon et al., 2003; van Dongen et al., 2019).

Our analysis of $[^{10}Be]_{measured}$ along the UM reveals consistently lower concentrations for coarse-grained (4–22.4 mm) compared to fine-grained (0.125–4 mm) UM samples (Figure 5a). Within the finer (< 16 mm) grain size sub-samples from UM2 and LM1 we observe no systematic variation (Figure 5c). Based on findings from fluvial landscapes, we assess below the relevance of (i) variable debris source areas and glacial transport, as well as (ii) erosive processes within glacial landscapes, as potential controls on our grain size effects in $[^{10}Be]_{measured}$ from Glacier d'Otemma.

(i) Differences in headwall lithology, debris origin or transport may result in selective contributions of grains with different $[^{10}Be]$. However, we found no difference in mineral composition and no evidence that debris originated from other source areas such as valley side walls, lateral moraines, or even the glacier bed. The passive nature of debris transport downglacier prevents significant post-depositional mixing and temporal storage, hindering the sorting of supraglacial debris. Moreover, the lack of transport processes that abrade supraglacial debris impedes clast comminution. Therefore, we consider the impact of source area and transport-related processes on our grain size distributions negligible.

(ii) Erosion in high-alpine glacial environments occurs through frequent small-scale rock falls and by infrequent medium- to large-scale rock falls or avalanches (e.g., Anderson, 2000; Arsenault & Meigs, 2005; Boulton & Deynoux, 1981). Large events have the potential to excavate bedrock covering a wide depth range from high

TABLE 3 Modelled sample ages, burial depth and ^{10}Be concentrations accumulated during glacial transport ($[^{10}Be]_{transport}$), as well as derived ^{10}Be concentrations in the headwalls ($[^{10}Be]_{headwall}$) and apparent headwall erosion rates

Sample	Age[a] (years)	Burial depth[a,c] (m)	$[^{10}Be]_{transport}$[a] $\times 10^3$ (atoms g^{-1})	$[^{10}Be]_{transport}/[^{10}Be]_{measured}$ (%)	$[^{10}Be]_{headwall}$[b] $\times 10^3$ (atoms g^{-1}) $\pm$ 1σ	Apparent headwall erosion rate[d] (mm yr^{-1}) $\pm$ 1σ
Upper medial moraine (UM)						
Fine-grained samples						
UM1/f	45	0.0	1.37	25	4.16 $\pm$ 0.57	5.1 $\pm$ 0.8
UM2/f	77	0.0	2.36	32	5.04 $\pm$ 0.79	4.2 $\pm$ 0.7
UM3/f	103	−1.2	2.84	44	3.68 $\pm$ 0.57	5.8 $\pm$ 1.0
UM4/f	130	−5.0	2.52	7	35.80 $\pm$ 1.86	0.6 $\pm$ 0.1
UM5/f	148	−9.1	2.35	21	8.61 $\pm$ 0.78	2.5 $\pm$ 0.3
UM6/f	167	−12.4	2.33	15	13.19 $\pm$ 0.98	1.6 $\pm$ 0.2
UM7/f	182	−14.7	2.36	9	23.98 $\pm$ 1.74	0.9 $\pm$ 0.1
UM8/f	199	−16.2	2.43	12	17.89 $\pm$ 1.23	1.2 $\pm$ 0.1
UM9/f	206	−16.7	2.47	13	16.12 $\pm$ 1.14	1.3 $\pm$ 0.1
Coarse-grained samples						
UM1/c	45	0.0	1.37	37	2.32 $\pm$ 0.47	9.1 $\pm$ 2.0
UM3/c	103	−1.2	2.84	94	0.17 $\pm$ 0.38	n.a.[e] $\pm$ n.a.[e]
UM4/c	130	−5.0	2.52	56	1.96 $\pm$ 0.44	10.8 $\pm$ 2.6
UM5/c	148	−9.1	2.35	31	5.12 $\pm$ 0.76	4.1 $\pm$ 0.7
UM7/c	182	−14.7	2.36	18	10.70 $\pm$ 0.89	2.0 $\pm$ 0.2
UM9/c	206	−16.7	2.47	14	14.57 $\pm$ 1.00	1.5 $\pm$ 0.2
Grain size sub-samples						
UM2/0.8	77	0.0	2.36	25	6.98 $\pm$ 1.18	3.0 $\pm$ 0.6
UM2/2	77	0.0	2.36	29	5.93 $\pm$ 0.82	3.6 $\pm$ 0.6
UM2/4	77	0.0	2.36	43	3.10 $\pm$ 0.51	6.8 $\pm$ 1.3
UM2/8	77	0.0	2.36	24	7.34 $\pm$ 0.69	2.9 $\pm$ 0.4
UM2/16	77	0.0	2.36	131	−0.56 $\pm$ 0.34	n.a.[e] $\pm$ n.a.[e]
Lower medial moraine (LM)						
Fine-grained samples						
LM1/f	35	0.0	1.05	6	16.73 $\pm$ 1.14	1.3 $\pm$ 0.1
LM2/f	67	0.0	2.04	9	20.33 $\pm$ 1.39	1.1 $\pm$ 0.1
LM3/f	94	0.0	2.84	22	10.25 $\pm$ 1.32	2.2 $\pm$ 0.3
LM4/f	115	−0.2	3.43	27	9.23 $\pm$ 1.10	2.4 $\pm$ 0.3
LM5/f	134	−1.8	3.46	24	11.23 $\pm$ 0.99	2.0 $\pm$ 0.2
LM6/f	152	−4.2	3.26	11	27.55 $\pm$ 2.00	0.8 $\pm$ 0.1
Grain size sub-samples						
LM1/0.8	35	0.0	1.05	7	14.23 $\pm$ 1.26	1.6 $\pm$ 0.2
LM1/2	35	0.0	1.05	6	15.23 $\pm$ 1.06	1.5 $\pm$ 0.2
LM1/4	35	0.0	1.05	5	19.92 $\pm$ 1.10	1.1 $\pm$ 0.1
LM1/8	35	0.0	1.05	6	17.17 $\pm$ 1.08	1.3 $\pm$ 0.1
LM1/16	35	0.0	1.05	8	12.18 $\pm$ 1.14	1.8 $\pm$ 0.2

[a]Computed using a simple 1D debris particle trajectory model (Wetterauer et al., 2022).
[b]Calculated by subtracting $[^{10}Be]_{transport}$ from $[^{10}Be]_{measured}$. 1σ estimates correspond to analytical uncertainties of $[^{10}Be]_{measured}$.
[c]Maximum burial depth modelled for debris particles of a sample. Negative numbers indicate partially englacial transport, zero indicates exclusively supraglacial transport.
[d]Calculated using spallogenic mean source area production rates of $P_{sp}(0) = 39.44$ atoms g^{-1} yr^{-1} and $P_{sp}(0) = 40.43$ atoms g^{-1} yr^{-1} and mean source area absorption mean free paths of $\Lambda = 142.56$ g cm^{-2} and $\Lambda = 144.80$ g cm^{-2} for UM and LM samples, respectively. 1σ estimates are based on the analytical uncertainties of $[^{10}Be]_{measured}$.
[e]Values not available (n.a.) due to unreasonable $[^{10}Be]_{headwall}$ estimates (see Section 5.2).

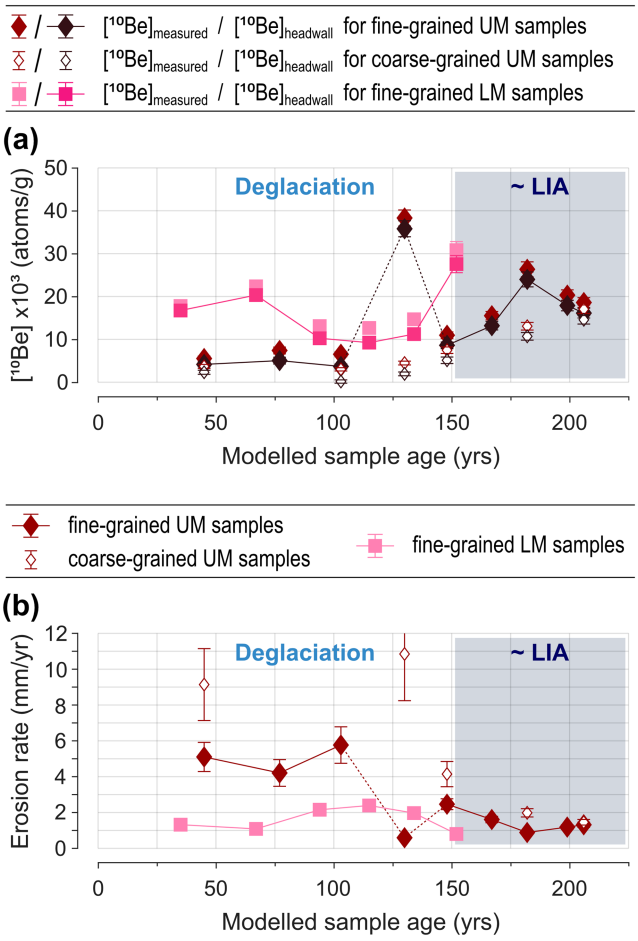

FIGURE 6 Medial moraine data of Glacier d'Otemma through time. (a) Comparison of $[^{10}Be]_{measured}$ and transport-corrected $[^{10}Be]_{headwall}$ ($\pm 1\sigma$ analytical error). (b) Apparent headwall erosion rates ($\pm 1\sigma$ uncertainty). Concentrations and rates are plotted against modelled sample ages. The end of the LIA and the following deglaciation are indicated. For clarity symbols of coarse-grained UM samples are smaller and unconnected. For fine-grained UM samples, the connecting line to the high concentration outlier UM4/f is dashed (see Section 6.2). Note that we did not calculate an erosion rate for the coarse-grained sample UM3 (see Section 5.2) and that symbol sizes are often larger than the provided error. UM/LM, upper/lower medial moraine; LIA, Little Ice Age [Color figure can be viewed at wileyonlinelibrary.com]

TABLE 4 Computed headwall ^{10}Be production rates and absorption mean free paths for three different time slices

Year	Mean ^{10}Be production rate (atoms g^{-1} yr^{-1}) $\pm 1\sigma$	Mean absorption mean free path (g cm^{-2})	Mean slope (deg)
Upper medial moraine (UM) headwalls			
2010	37.88 ± 2.58	144.59	35
1973	39.44 ± 2.30	142.56	43
1850	39.44 ± 2.30	142.56	43
Lower medial moraine (LM) headwalls			
2010	39.85 ± 2.81	146.14	32
1973	40.43 ± 2.65	144.80	36
1850	41.92 ± 2.62	142.46	42

$[^{10}Be]$ at the surface down to low $[^{10}Be]$ at depth (Niemi et al., 2005). Distinguishing between supraglacial sand, pebbles and < 30 cm-sized blocks, Sarr et al. (2019) found no significant size-dependent variation in $[^{10}Be]$. They argue that the distribution of supraglacial clast sizes from sand to boulders results from numerous rock impacts over long fall distances (Ruiz-Carulla et al., 2017), and thus, is independent of their initial depth within the rock wall. However, their findings are based on only two moraine samples from different glaciers in the Mont Blanc Massif. These samples were taken close to the glacier terminus, one of which actually reveals slightly decreasing $[^{10}Be]$ from sand to cobble to blocks. We note that supraglacial debris near termini is generally more susceptible to mixing as debris is compressed due to declining ice surface velocities (Anderson et al., 2021), and basal debris input is also more likely near the terminus (Boulton, 1978). Therefore, termini samples may indeed show grain-size $[^{10}Be]$ patterns different from our samples. Depending on the magnitude of rock falls, we actually do think that larger events are also more likely composed of coarser and more deeply anchored material compared to smaller events. Although rocks detaching from headwalls typically shatter upon impact, the resulting clast sizes are partly determined by bedrock properties (e.g., discontinuities, joint patterns, rock strength; see e.g., Ruiz-Carulla et al., 2015, 2017). Moreover, models on frost weathering processes indicate that the magnitude of frost damage decreases with depth into the rock wall (e.g., Rempel et al., 2016) and, hence, relatively fewer fractures may be expected at greater depth than near the surface.

Therefore, we propose that higher $[^{10}Be]$ in the fine fraction reflect a higher proportion of fine superficial material frequently chipped off the headwall by near-steady exhumation. The coarse fraction may comprise relatively more coarse material of lower $[^{10}Be]$ from greater depth within the bedrock. Importantly, both grain size fractions (0.125–4 and 4–22.4 mm) reproduce a comparable and fairly consistent downglacier $[^{10}Be]$ pattern (Figure 5a), indicating that processes accounting for this effect cannot have changed by much over the transport time invoked here. If our record was affected by extensive rock falls or rock avalanches, low concentration outliers should be present. Also, outlines of rock fall deposits can often be delineated on glaciers (e.g., Deline, 2009), in the field or from remote sensing products, which we did not observe on UM and LM.

6.2 | Temporal variations in apparent headwall erosion rates

Our $[^{10}Be]$ from Glacier d'Otemma show systematic variations downglacier, and thus, variations with time. In particular, along both our fine- and coarse-grained UM records, $[^{10}Be]$ generally decrease over the last ~200 years (Figure 6a), suggesting that erosion rates increased towards the present (Figure 6b). We consider the fine-grained sample UM4/f as an outlier, given that the coarse-grained sample UM4/c fits the temporal systematics of the record well and that the deviation between the two size fractions is large (Figure 5a). In the following, we will address the question whether the decreasing nuclide concentrations really reflect an overall acceleration in headwall erosion through time. Later, we (i) inspect the reliability of our derived erosion rates with respect to cosmogenic steady state, and then (ii) focus both on processes modulating headwall erosion in a

deglaciating landscape and (iii–iv) on conditions controlling the nuclide history of the rock itself.

(i) Under the assumption implied by Equation 1 that headwall surfaces erode steadily and uniformly, $[^{10}Be]_{headwall}$ from UM and LM samples translate into erosion rates between 0.6 and 10.8 mm yr^{-1} (Table 3). With an average attenuation length of ~54 cm for the headwalls of Petit Mont Collon and erosion rates of ~1 to 2 mm yr^{-1} it would take at least ~540 to 270 years to reach cosmogenic steady state. However, our estimated sample ages are younger and large parts of the source areas experienced ice cover retreat after the LIA, which argues against cosmogenic steady state. Still, source areas exposed during the LIA were most likely also exposed for centuries before, as glaciers were smaller prior to the LIA (e.g., Holzhauser et al., 2005), making cosmogenic steady state possible. We therefore consider samples older than ~150 years with erosion rates of 0.9 to 2.0 mm yr^{-1} (UM6–UM9) to be the most reliable (Figure 6b). Samples younger than the LIA, with erosion rates of up to 10.8 mm yr^{-1}, should be treated with caution (Figure 6b). Overall reliability is supported by other studies from the European Alps that derive similar cosmogenic nuclide-based erosion rates for rock walls close to glacier surfaces (Mont Blanc massif: ~0.1 to 1.1 mm yr^{-1}, Sarr et al., 2019; Eiger Mountain: ~1.7 and ~2.6 mm yr^{-1}, Mair et al., 2019, 2020) and for glacial catchments (Glacier du Mont Miné: ~1.8 to 6.4 mm yr^{-1}, Wittmann et al., 2007). Moreover, our estimates compare well to headwall erosion rates from medial moraine debris in the Alaska Range (~0.5 to 1.3 mm yr^{-1}; Ward & Anderson, 2011) and the Indian Himalaya (~0.6 to 1.3 mm yr^{-1}; Scherler & Egholm, 2020).

(ii) The tendency towards higher recent erosion rates may be indicative of a transient landscape that responds to deglaciation with faster erosion. Rock fall inventories from the European Alps indicate that periods of higher temperatures after the LIA between 1900 and 2010 coincide with enhanced rock fall activity, particularly in areas of thawing permafrost (Huggel et al., 2012; Ravanel & Deline, 2009, 2011). Enhanced rock fall coincides with summer heat waves (2003 and 2015), likely caused by a warming-related deepening of the active layer (Gruber et al., 2004; Ravanel et al., 2017). At the Kitzsteinhorn, Hartmeyer et al. (2020a, 2020b) identified that the majority of rock detachments adjacent to a thinning glacier occur within recently uncovered rock walls < 20 m above the glacier surface. The authors attribute the increased rock fall activity to a combination of thermo-mechanical stresses and active layer penetration into the rock. Similarly, recently exposed bedrock at Glacier d'Otemma could be prone to enhanced rock fall, since the headwall-ice-contact zone at Petit Mont Collon experienced up to ~50 m of ice loss since 1850 (Figure 4 in Lambiel & Talon, 2019).

(iii) The longer the downglacier debris transport continues, the longer it may be exposed to additional cosmic radiation, and the more additional ^{10}Be accumulation may contribute to $[^{10}Be]_{measured}$. At present, debris transport on Glacier d'Otemma proceeds slowly (Figure S2) and exclusively supraglacially (Figure S7). Nonetheless, our computation of downglacier debris trajectories through time indicates that debris burial and shielding in the past have been sufficient to keep $[^{10}Be]_{transport}$ low (Figure 6a). This is in line with estimates from Ward and Anderson (2011) and Scherler and Egholm (2020). Moreover, downglacier medial moraine samples may be a composite of different debris sources as debris continuously emerges in the ablation zone, and their ^{10}Be signatures may differ depending on where along the source area debris deposition occurred. Recently, at the UM, debris input appears to be a point source (Figure 2), as simulated with our model. At the LM, debris delivery may occur along a wider zone (Figure 2), which cannot be resolved with our model. However, potential differences, at present and in the past, are presumably small as the debris source area is isolated and not very extensive. Therefore, we exclude transport time and other additional debris sources as a possible explanation for the observed systematic temporal variation in $[^{10}Be]_{measured}$.

(iv) The steady retreat of Glacier d'Otemma and concurrent deglaciation of Petit Mont Collon uncover headwall sections that presently deliver rocks to the glacier (Figure 7). Newly exposed debris source areas following the LIA could affect the $[^{10}Be]_{headwall}$ in our samples in two ways. First, as the glacier surface lowers through time, the debris source area expands towards lower elevations (Figure 4), where production rates are lower. Therefore, computed mean source area production rates decrease towards the present (Table 4 and Figure 3b–d). However, since headwall elevation ranges are small, production rates differ by only up to 5%, too low to explain the substantial temporal $[^{10}Be]$ changes alone. Second, deglaciation also exposes bedrock areas previously shielded from cosmic radiation by ice. These areas possibly inherit nuclide signatures from previous episodes of exposure during the Holocene, as the LIA was preceded by periods of major glacier recession (e.g., Holzhauser et al., 2005). If subglacial erosion has removed a substantial amount of bedrock from these areas during the LIA, present-day $[^{10}Be]_{headwall}$ may be lower compared to areas which have been ice-free over centuries. Instead, if subglacial erosion was negligible and if headwall erosion during former ice-free times proceeded slowly, $[^{10}Be]_{headwall}$ at those surfaces may be even higher (e.g., a possible scenario for the high concentration outlier UM4/f, Figure 6a). As a consequence, continued source area expansion with possibly variable $[^{10}Be]_{headwall}$ may progressively dilute the previous signatures from LIA times and may result in time-dependent $[^{10}Be]_{headwall}$ variations. However, whether this would result in generally higher or lower nuclide concentrations is currently difficult to evaluate.

6.3 | Medial moraines in comparison

When compared through time, UM and LM $[^{10}Be]_{headwall}$ are surprisingly different (Table 3 and Figure 6a). Overall, LM $[^{10}Be]_{headwall}$ are higher for samples similar in age and the difference to the UM amounts to > 10^4 atoms g^{-1} for samples younger than ~80 years, but no systematic temporal difference is evident. The only obvious difference between the two medial moraines is that they have different source headwalls (Figure 2, see Section 3.2). Yet, lithology is uniform across the source headwalls and average ^{10}Be production rates vary by only up to 6% and are thus insufficient to explain the observed differences in $[^{10}Be]_{headwall}$ (Table 4 and Figure 3b–d). Also, the processing of both UM and LM samples has been comparable, and we could not observe any obvious differences in the sampled grain size distribution (Figure S1), or in the mineral composition. Hence, we inspect (i) differences in solar insolation due to different aspects and (ii) different deglaciation histories as potential causes.

(i) The aspect of rock faces has been used to explain distinct spatial patterns of rock fall and rock wall erosion, as it affects the

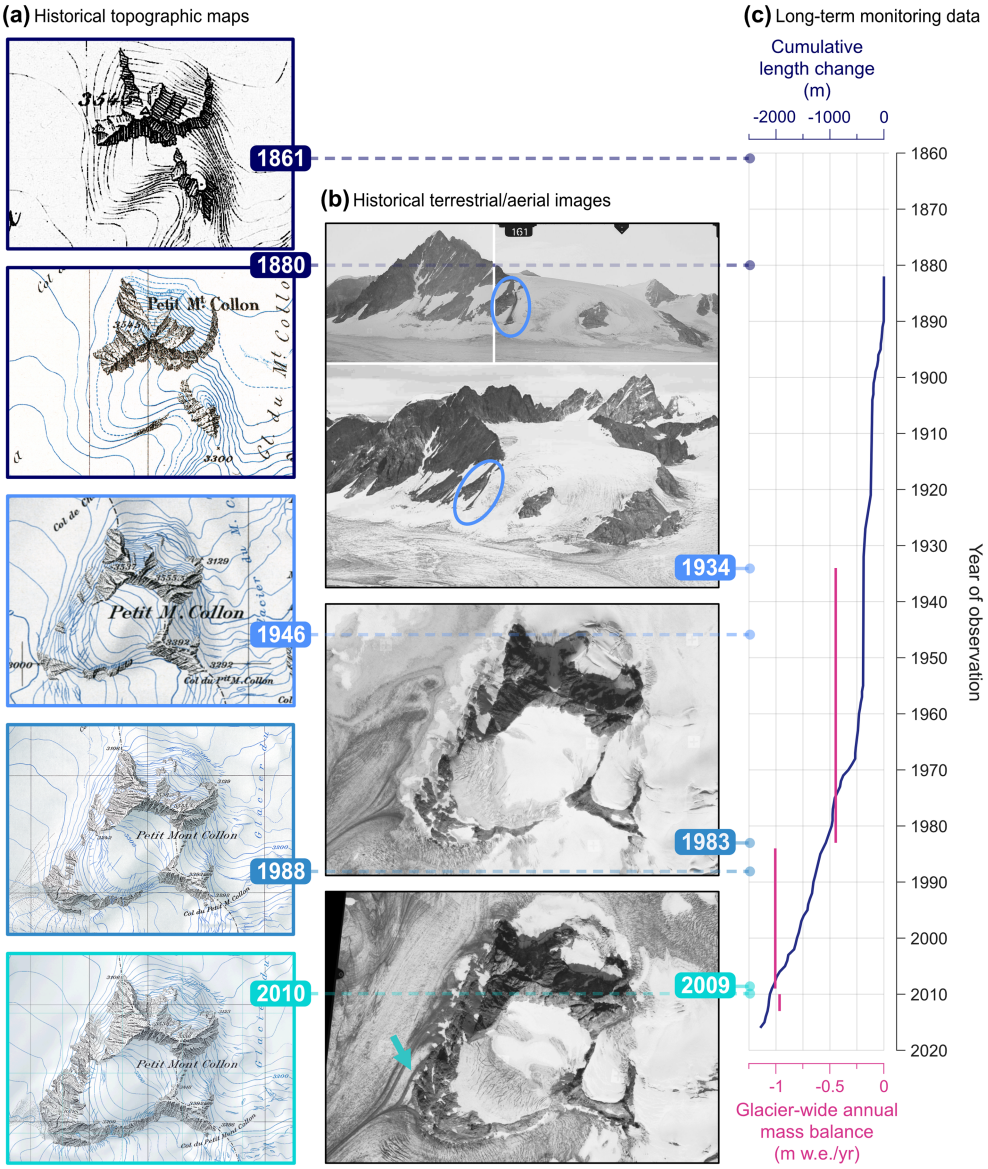

FIGURE 7 Chronological overview on available historical datasets from Petit Mont Collon used to assess the deglaciation history of the debris source area and to define the setup of our debris trajectory model. (a) Topographic maps of ice cover retreat across the headwalls. Note the disconnection of ice, formerly feeding into the glacier's main trunk and evolving into an isolated glacier in the centre of Petit Mont Collon (topographic maps by swisstopo, 2021). (b) Terrestrial and aerial snapshots picturing the exposure of formerly ice-covered bedrock. The recent uncovering is patchier for headwalls to the lower medial moraine. Note the small-scale rock fall captured on the 1934 photographs (encircled), representative for erosion processes operating frequently in high-alpine glacial environments, and the ice septum separating the two moraines (arrowed) (historical images by swisstopo, 2021). (c) Long-term monitoring records of glacier retreat and decline in annual glacier-wide mass balance of Glacier d'Otemma (GLAMOS, 2019a, 2019b). (m w.e. yr^{-1}, metre water equivalent per year) [Color figure can be viewed at wileyonlinelibrary.com]

moisture level and the thermo-mechanical regime of rock walls (e.g., Coutard & Francou, 1989; Sass, 2005). Gruber et al. (2004) associate increased erosive activity during the hot summer of 2003 with an increase of permafrost thawing depth. They explain larger thaw anomalies on north-facing rock walls with lower inter-annual variability of thawing depth due to less direct solar radiation than south-facing rock walls. Similarly, studies by Sass (2007, 2010) suggest enhanced Holocene rock wall erosion and present-day rock falls at northerly oriented rock walls. At Petit Mont Collon, the west-northwest facing UM headwalls most likely experience different insolation and temperatures than the south-southwest facing LM headwalls. Permafrost is more extensive and thicker at UM headwalls but rather patchy across LM headwalls (BAFU, 2005). In addition, mean slope angles of UM headwalls appear to be steeper, by up to ~20%, during deglaciation following the LIA (Table 4). We note, however, that this difference strongly depends on the accuracy of the glacier outlines used. Nonetheless, in this context, recently faster erosion of UM compared to LM headwalls due to northerly exposure and possibly steeper slopes appears reasonable (Figure 6b).

(ii) Ice cover retreat across Petit Mont Collon has proceeded unequally after the LIA (Figure 7a,b). It appears that UM headwalls experience a comparatively steady bedrock exposure due to glacier thinning, which may be expressed in the more systematic temporal [^{10}Be] variation along the UM. In contrast, LM headwalls are additionally affected by the disintegration of a small glacier that separated from Glacier d'Otemma upwards onto Petit Mont Collon. This detachment proceeds unevenly and leads to a rather patchy exposure of previously ice-covered bedrock, which may thus manifest itself in the less distinct [^{10}Be] variation along the LM.

In summary, we attribute the more recent differences in UM and LM [^{10}Be] to a combination of spatial differences in headwall erosion rates and ice cover retreat across Petit Mont Collon. Spatially varying erosion rates across formerly glaciated bedrock surfaces have previously been observed in the Mont Blanc Massif (Lehmann et al., 2020). Further, the presence or absence of ice cover is known to modulate the nuclide concentrations inherited from previous exposure (e.g., Cockburn & Summerfield, 2004). However, due to the centennial coverage of our dataset, whether $[^{10}Be]_{headwall}$ prior to the LIA were higher or lower than today, and whether they were preserved throughout ice coverage or reduced or even reset by subglacial erosion (see Section 6.2) remain open questions.

6.4 | Methodological conclusions and future opportunities

Our findings from Glacier d'Otemma show decreasing [^{10}Be] and increasing erosion rates towards the present, in accordance with observations by Scherler and Egholm (2020) from a Himalayan glacier. Systematic instead of random downglacier [^{10}Be] variations in both studies support the notion that medial moraines can be exploited as archives of headwall erosion above glaciers. This is reinforced by the fact that the observed downglacier [^{10}Be] trend is reflected in two different size fractions. Therefore, cosmogenic nuclide-based medial moraine records appear to reflect observations of decadal changes in headwall erosion (e.g., Hartmeyer et al., 2020a, 2020b) on centennial timescales, but encounter limitations on shorter timescales due to the nuclide integration time (see Section 6.2). To further elaborate on climate change-related responses of headwalls and adjacent debris-covered glaciers, future analyses may involve various glacial catchments and debris source areas that differ in size, orientation or morphology to check for potential spatial patterns. Besides, consulting additional temporal records on rock wall temperatures or water availability may be of interest, too, since studies indicate that increased meltwater and rainwater runoff may enhance the frost weathering efficacy in the contact zone of headwall and glacier (Hartmeyer et al., 2020a, 2020b) and that warmer temperatures after the LIA may have enhanced the frost cracking efficiency (Mair et al., 2020), both preconditioning rock-fracturing.

Applying our particle trajectory model indicates that the model-based ^{10}Be corrections due to downglacier transport are in most cases not very substantial (Figure 6a). Yet, resolving slow supraglacial transport close to the headwalls with a simple 1D model proved to be challenging (see Section S4.2.1). Whereas older englacially transported samples largely remain unaffected by this, younger almost exclusively supraglacially transported samples may be affected more severely by the assumptions and uncertainties underlying the model (see Sections 5.2 and S4.2.5). Using a well calibrated three-dimensional (3D) glacier model may help to overcome these limitations in future studies, to refine ^{10}Be corrections and sample age estimates, and to backtrack particles more precisely to specific delivery zones within a source area (e.g., certain elevation windows).

We further suggest that the manual amalgamation of sand-sized supraglacial debris offers the opportunity to obtain representative estimates of headwall erosion rates, as the analysis of [^{10}Be] from various fine-grained sub-samples of UM2 and LM1 revealed no obvious dependency of size fractions < 16 mm. However, on a larger scale, systematic grain size differences exist when comparing sand-sized (0.125–4 mm) and pebble-sized (4–22.4 mm) debris fractions of several samples, with the latter having consistently lower [^{10}Be] (see Section 6.1). These trends need further investigation by future studies.

Finally, the choice of a glacier with a small catchment, as is the case for Glacier d'Otemma, holds several advantages. The debris of both medial moraines can be traced to the well-definable headwalls of Petit Mont Collon. The small size and homogeneity of the debris source area reduce complexity. Differences in [^{10}Be] production rates are small, due to the small elevation range, and lithology can be excluded as a primary factor for temporal and spatial variability in headwall erosion. Yet, disentangling cosmogenic signals of headwall erosion from those rooted in the nuclide history of deglaciating bedrock itself, both governing $[^{10}Be]_{headwall}$, remains challenging (see Sections 6.2 and 6.3). Field sites with debris source areas that are characterized by a simple bedrock exposure history may help to clarify these issues in the future.

7 | CONCLUSIONS

We derived a ~200-year record of headwall erosion rates at Glacier d'Otemma, Switzerland, from combining cosmogenic ^{10}Be concentration ([^{10}Be]) measurements on medial moraine debris with particle trajectory and age modelling. Our results indicate that downglacier [^{10}Be] vary systematically with time. During the LIA (debris samples older than ~150 years), we find relatively high [^{10}Be] yielding low apparent headwall erosion rates of 0.9 to 2.0 mm yr^{-1}. After the LIA (debris samples younger than ~150 years), lower [^{10}Be] result in higher apparent headwall erosion rates of up to 10.8 mm yr^{-1}. This decrease in [^{10}Be] from past to present is reflected both in sand-sized and pebble-sized grain size fractions, which suggests that the temporal trends are not affected by large stochastic events that could bias cosmogenic nuclide concentrations.

Computing debris particle trajectories through the glacier from source area to sample location with our model shows that the observed temporal variation in [^{10}Be] still remains after correcting for additional nuclide accumulation during glacial transport. Recently decreasing [^{10}Be] seem to reflect a combination of processes that can be associated with the ongoing ice cover retreat across the source headwalls since the end of the LIA. On the one hand, high-alpine headwalls face increased destabilization and retreat as glaciers degrade and permafrost thaws. On the other hand, they experience profound changes in shielding and exposure to cosmic rays as ice cover disintegrates and debris source areas expand. Temporal differences in [^{10}Be] along two parallel medial moraines suggest that both headwall orientation and their deglaciation history are important factors to consider when interpreting medial moraine cosmogenic nuclide concentrations.

ACKNOWLEDGEMENTS

This research was funded from the European Research Council (ERC) under the European Union's Horizon 2020 research and innovation programme (grant agreement number 759639). The authors are grateful to the 'COLD'-project members Donovan Dennis and Deniz Gök for scientific discussions and support during sampling. Stefan Heinze and Steven Binnie from the University of Cologne are thanked for performing AMS measurements. Swisstopo and GLAMOS are acknowledged for giving access to historical datasets. Cathrin Schulz, Nadja Kuhl and Kristina Krüger are thanked for their help and advice in sample preparation. The authors also thank two anonymous reviewers and the editors for their constructive and thoughtful feedback that improved this manuscript. Open access funding enabled and organized by Projekt DEAL.

CONFLICT OF INTEREST

The authors declare no conflicts of interest.

FUNDING INFORMATION

European Research Council (ERC) H2020-EU.1.1.; Grant Agreement Number 759639; Project 'COLD – Climate Sensitivity of Glacial Landscape Dynamics'.

AUTHOR CONTRIBUTIONS

KW carried out sample collection, sample preparation, data evaluation, and modelling. DS conceived and supervised the project, derived the remotely-sensed glacier surface velocities, and was the main advisor during sample collection, data evaluation and modelling. LSA supported sample collection and was available for discussion during data evaluation and modelling. HW was the main advisor during sample preparation and responsible for the *in situ* ^{10}Be laboratory training. KW prepared the initial draft, figures and tables and adjusted the manuscript based on the comments and edits of DS, LSA and HW.

DATA AVAILABILITY STATEMENT

The cosmogenic nuclide and model data of this study and a detailed description of the sample processing and debris trajectory modelling are available in the accompanying data publication Wetterauer et al. (2022), https://doi.org/10.5880/GFZ.3.3.2021.007. These data are freely available under the Creative Commons Attribution 4.0 International (CC BY 4.0) open access license at GFZ Data Services. When using these data please cite this article.

ORCID

Katharina Wetterauer https://orcid.org/0000-0002-2937-5856
Dirk Scherler https://orcid.org/0000-0003-3911-2803
Leif S. Anderson https://orcid.org/0000-0003-3134-1775
Hella Wittmann https://orcid.org/0000-0002-1252-7059

REFERENCES

Aguilar, G., Carretier, S., Regard, V., Vassallo, R., Riquelme, R. & Martinod, J. (2014) Grain size-dependent ^{10}Be concentrations in alluvial stream sediment of the Huasco Valley, a semi-arid Andes region. *Quaternary Geochronology*, 19, 163–172. Available from: https://doi.org/10.1016/j.quageo.2013.01.011

Alley, R.B., Cuffey, K.M., Evenson, E.B., Strasser, J.C., Lawson, D.E. & Larson, G.J. (1997) How glaciers entrain and transport basal sediment: Physical constraints. *Quaternary Science Reviews*, 16(9), 1017–1038. Available from: https://doi.org/10.1016/S0277-3791(97)00034-6

Anderson, L.S. & Anderson, R.S. (2016) Modeling debris-covered glaciers: response to steady debris deposition. *The Cryosphere*, 10(3), 1105–1124. Available from: https://doi.org/10.5194/tc-10-1105-2016

Anderson, L.S., Armstrong, W.H., Anderson, R.S., Scherler, D. & Petersen, E. (2021) The Causes of Debris-Covered Glacier Thinning: Evidence for the Importance of Ice Dynamics From Kennicott Glacier, Alaska. *Frontiers in Earth Science*, 9, 1–19. Available from: https://doi.org/10.3389/feart.2021.680995

Anderson, R.S. (2000) A model of ablation-dominated medial moraines and the generation of debris-mantled glacier snouts. *Journal of Glaciology*, 46(154), 459–469. Available from: https://doi.org/10.3189/172756500781833025

Arsenault, A.M. & Meigs, A.J. (2005) Contribution of deep-seated bedrock landslides to erosion of a glaciated basin in southern Alaska. *Earth Surface Processes and Landforms*, 30(9), 1111–1125. Available from: https://doi.org/10.1002/esp.1265

Balco, G., Stone, J.O., Lifton, N.A. & Dunai, T.J. (2008) A complete and easily accessible means of calculating surface exposure ages or erosion rates from ^{10}Be and ^{26}Al measurements. *Quaternary Geochronology*, 3(3), 174–195. Available from: https://doi.org/10.1016/j.quageo.2007.12.001

Ballantyne, C.K. (2002) A general model of paraglacial landscape response. *The Holocene*, 12(3), 371–376. Available from: https://doi.org/10.1191/0959683602hl553fa

Belmont, P., Pazzaglia, F.J. & Gosse, J.C. (2007) Cosmogenic ^{10}Be as a tracer for hillslope and channel sediment dynamics in the Clearwater River, western Washington State. *Earth and Planetary Science Letters*, 264(1-2), 123–135. Available from: https://doi.org/10.1016/j.epsl.2007.09.013

Benn, D.I., Bolch, T., Hands, K., Gulley, J., Luckman, A., Nicholson, L.I., Quincey, D., Thompson, S., Toumi, R. & Wiseman, S. (2012) Response of debris-covered glaciers in the Mount Everest region to recent warming, and implications for outburst flood hazards. *Earth-Science Reviews*, 114(1–2), 156–174. Available from: https://doi.org/10.1016/j.earscirev.2012.03.008

Benn, D.I. & Evans, D.J.A. (1998) *Glaciers and glaciation*. London: Arnold.

Bolch, T., Buchroithner, M., Pieczonka, T. & Kunert, A. (2008) Planimetric and volumetric glacier changes in the Khumbu Himal, Nepal, since 1962 using Corona, Landsat TM and ASTER data. *Journal of Glaciology*, 54(187), 592–600. Available from: https://doi.org/10.3189/002214308786570782

Borchers, B., Marrero, S., Balco, G., Caffee, M., Goehring, B., Lifton, N., Nishiizumi, K., Phillips, F., Schaefer, J. & Stone, J. (2016) Geological calibration of spallation production rates in the CRONUS-Earth project. *Quaternary Geochronology*, 31, 188–198. Available from: https://doi.org/10.1016/j.quageo.2015.01.009

Boulton, G.S. (1978) Boulder shapes and grain size distributions of debris as indicators of transport paths through a glacier and till genesis. *Sedimentology*, 25(6), 773–799. Available from: https://doi.org/10.1111/j.1365-3091.1978.tb00329.x

Boulton, G.S. & Deynoux, M. (1981) Sedimentation in glacial environments and the identification of tills and tillites in ancient sedimentary sequences. *Precambrian Research*, 15(3-4), 397–422. Available from: https://doi.org/10.1016/0301-9268(81)90059-0

Boulton, G.S. & Eyles, N. (1979) Sedimentation by valley glaciers: a model and genetic classification. In: Schlüchter, C. (Ed.) *Moraines and Varves*. Rotterdam, A.A: Balkema, pp. 11–23.

Braithwaite, R.J. (2015) From Doktor Kurowski's Schneegrenze to our modern glacier equilibrium line altitude (ELA). *The Cryosphere*, 9(6), 2135–2148. Available from: https://doi.org/10.5194/tc-9-2135-2015

Brown, E.T., Stallard, R.F., Larsen, M.C., Bourlès, D.L., Raisbeck, G.M. & Yiou, F. (1998) Determination of predevelopment denudation rates of an agricultural watershed (Cayaguás River, Puerto Rico) using in-situ-produced ^{10}Be in river-borne quartz. *Earth and Planetary Science Letters*, 160(3–4), 723–728. Available from: https://doi.org/10.1016/S0012-821X(98)00123-X

Brown, E.T., Stallard, R.F., Larsen, M.C., Raisbeck, G.M. & Yiou, F. (1995) Denudation rates determined from the accumulation of in situ-produced ^{10}Be in the luquillo experimental forest, Puerto Rico. *Earth and Planetary Science Letters*, 129(1–4), 193–202. Available from: https://doi.org/10.1016/0012-821X(94)00249-X

Bundesamt für Umwelt BAFU. (2005) Hinweiskarte der potenziellen Permafrostverbreitung. Available from: https://map.geo.admin.ch. (Accessed: 21/05/2021).

Carretier, S., Regard, V. & Soual, C. (2009) Theoretical cosmogenic nuclide concentration in river bed load clasts: Does it depend on clast size? *Quaternary Geochronology*, 4(2), 108–123. Available from: https://doi.org/10.1016/j.quageo.2008.11.004

Chmeleff, J., von Blanckenburg, F., Kossert, K. & Jakob, D. (2010) Determination of the ^{10}Be half-life by multicollector ICP-MS and liquid scintillation counting. *Nuclear Instruments and Methods in Physics Research B: Beam Interactions with Materials and Atoms*, 268(2), 192–199. Available from: https://doi.org/10.1016/j.nimb.2009.09.012

Cockburn, H.A.P. & Summerfield, M.A. (2004) Geomorphological applications of cosmogenic isotope analysis. *Progress in Physical Geography: Earth and Environment*, 28(1), 1–42. Available from: https://doi.org/10.1191/0309133304pp395oa

Cossart, E., Braucher, R., Fort, M., Bourlès, D.L. & Carcaillet, J. (2008) Slope instability in relation to glacial debuttressing in alpine areas (Upper Durance catchment, southeastern France): Evidence from field data and ^{10}Be cosmic ray exposure ages. *Geomorphology*, 95(1–2), 3–26. Available from: https://doi.org/10.1016/j.geomorph.2006.12.022

Coutard, J.-P. & Francou, B. (1989) Rock temperature measurements in two alpine environments: implications for frost shattering. *Arctic and Alpine Research*, 21(4), 399–416. Available from: https://doi.org/10.2307/1551649

Deline, P. (2005) Change in surface debris cover on Mont Blanc massif glaciers after the 'Little Ice Age' termination. *The Holocene*, 15(2), 302–309. Available from: https://doi.org/10.1191/0959683605hl809rr

Deline, P. (2009) Interactions between rock avalanches and glaciers in the Mont Blanc massif during the late Holocene. *Quaternary Science Reviews*, 28(11–12), 1070–1083. Available from: https://doi.org/10.1016/j.quascirev.2008.09.025

Dewald, A., Heinze, S., Jolie, J., Zilges, A., Dunai, T., Rethemeyer, J., Melles, M., Staubwasser, M., Kuczewski, B., Richter, J., Radtke, U., von Blanckenburg, F. & Klein, M. (2013) CologneAMS, a dedicated center for accelerator mass spectrometry in Germany. *Nuclear Instruments and Methods in Physics Research Section B: Beam Interactions with Materials and Atoms*, 294, 18–23. Available from: https://doi.org/10.1016/j.nimb.2012.04.030

Dunne, J., Elmore, D. & Muzikar, P. (1999) Scaling factors for the rates of production of cosmogenic nuclides for geometric shielding and attenuation at depth on sloped surfaces. *Geomorphology*, 27(1–2), 3–11. Available from: https://doi.org/10.1016/S0169-555X(98)00086-5

Dyurgerov, M.B. (2002) Glacier mass balance and regime: data of measurements and analysis. In: Meier, M. & Armstrong, R. (Eds.) *Institute of Arctic and Alpine Research Occasional Paper No. 55*. Boulder, CO, USA: University of Colorado.

Eyles, N. & Rogerson, R.J. (1978a) A framework for the investigation of medial moraines formation: Austerdalsbreen, Norway, and Berendon Glacier, British Columbia, Canada. *Journal of Glaciology*, 20(82), 99–113. Available from: https://doi.org/10.3189/S0022143000021249

Eyles, N. & Rogerson, R.J. (1978b) Sedimentology of medial moraines on Berendon Glacier, British Columbia, Canada: implications for debris transport in a glacierized basin. *Geological Society of America Bulletin*, 89(11), 1688–1693. Available from: https://doi.org/10.1130/0016-7606(1978)89<1688:SOMMOB>2.0.CO;2

Farinotti, D., Huss, M., Fürst, J.J., Landmann, J., Machguth, H., Maussion, F. & Pandit, A. (2019) A consensus estimate for the ice thickness distribution of all glaciers on Earth. *Nature Geoscience*, 12(3), 168–173. Available from: https://doi.org/10.1038/s41561-019-0300-3

Fischer, M., Huss, M., Barboux, C. & Hoelzle, M. (2014) The new Swiss Glacier Inventory SGI2010: relevance of using high-resolution source data in areas dominated by very small glaciers. *Arctic, Antarctic, and Alpine Research*, 46(4), 933–945. Available from: https://doi.org/10.1657/1938-4246-46.4.933

Fischer, M., Huss, M. & Hoelzle, M. (2015) Surface elevation and mass changes of all Swiss glaciers 1980-2010. *The Cryosphere*, 9(2), 525–540. Available from: https://doi.org/10.5194/tc-9-525-2015

Fleischer, F., Otto, J.-C., Junker, R.R. & Hölbling, D. (2021) Evolution of debris cover on glaciers of the Eastern Alps, Austria, between 1996 and 2015. *Earth Surface Processes and Landforms*, 46(9), 1673–1691. Available from: https://doi.org/10.1002/esp.5065

Gabbi, J., Farinotti, D., Bauder, A. & Maurer, H. (2012) Ice volume distribution and implications on runoff projections in a glacierized catchment. *Hydrology and Earth System Sciences*, 16(12), 4543–4556. Available from: https://doi.org/10.5194/hess-16-4543-2012

GLAMOS. (2019a) Swiss Glacier Length Change, release 2019, Glacier Monitoring Switzerland. Available from: https://doi.org/10.18750/lengthchange.2019.r2019

GLAMOS. (2019b) Swiss Glacier Volume Change, release 2019, Glacier Monitoring Switzerland. Available from: https://doi.org/10.18750/volumechange.2019.r2019

GLAMOS. (2021) [homepage on the internet]. Glacier Monitoring Switzerland. Available from: https://www.glamos.ch. (Accessed: 21/05/2021).

Glasser, N.F., Holt, T.O., Evans, Z.D., Davies, B.J., Pelto, M. & Harrison, S. (2016) Recent spatial and temporal variations in debris cover on Patagonian glaciers. *Geomorphology*, 273, 202–216. Available from: https://doi.org/10.1016/j.geomorph.2016.07.036

Glen, J.W. (1952) Experiments on the deformation of ice. *Journal of Glaciology*, 2(12), 111–114. Available from: https://doi.org/10.3189/S0022143000034067

Glen, J.W. (1955) The creep of polycrystalline ice. *Proceedings of the Royal Society of London. Series A: Mathematical and Physical Sciences*, 228(1175), 519–538. Available from: https://doi.org/10.1098/rspa.1955.0066

Gomez, B. & Small, R.J. (1985) Medial moraines of the Haut Glacier d'Arolla, Valais, Switzerland: debris supply and implications for moraine formation. *Journal of Glaciology*, 31(109), 303–307. Available from: https://doi.org/10.3189/S0022143000006638

Gruber, S. & Haeberli, W. (2007) Permafrost in steep bedrock slopes and its temperature-related destabilization following climate change. *Journal of Geophysical Research*, 112(F2), F02S18. Available from: https://doi.org/10.1029/2006JF000547

Gruber, S., Hoelzle, M. & Haeberli, W. (2004) Permafrost thaw and destabilization of Alpine rock walls in the hot summer of 2003. *Geophysical Research Letters*, 31(13), L13504. Available from: https://doi.org/10.1029/2004GL020051

Guillon, H., Mugnier, J.-L., Buoncristiani, J.-F., Carcaillet, J., Godon, C., Prud'homme, C., van der Beek, P. & Vassallo, R. (2015) Improved discrimination of subglacial and periglacial erosion using ^{10}Be concentration measurements in subglacial and supraglacial sediment load of the Bossons glacier (Mont Blanc massif, France). *Earth Surface Processes and Landforms*, 40(9), 1202–1215. Available from: https://doi.org/10.1002/esp.3713

Haeberli, W. & Beniston, M. (1998) Climate change and its impacts on glaciers and permafrost in the Alps. *Ambio: A Journal of the Human Environment*, 27, 258–265.

Haeberli, W., Wegmann, M. & Vonder, M.D. (1997) Slope stability problems related to glacier shrinkage and permafrost degradation in the Alps. *Eclogae Geologicae Helvetiae*, 90, 407–414. Available from: https://doi.org/10.5169/seals-168172

Hartmeyer, I., Delleske, R., Keuschnig, M., Krautblatter, M., Lang, A., Schrott, L. & Otto, J.-C. (2020a) Current glacier recession causes significant rockfall increase: the immediate paraglacial response of deglaciating cirque walls. *Earth Surface Dynamics*, 8(3), 729–751. Available from: https://doi.org/10.5194/esurf-8-729-2020

Hartmeyer, I., Keuschnig, M., Delleske, R., Krautblatter, M., Lang, A., Schrott, L., Prasicek, G. & Otto, J.-C. (2020b) A 6-year lidar survey reveals enhanced rockwall retreat and modified rockfall magnitudes/frequencies in deglaciating cirques. *Earth Surface Dynamics*, 8(3), 753–768. Available from: https://doi.org/10.5194/esurf-8-753-2020

Heimsath, A.M. & McGlynn, R. (2008) Quantifying periglacial erosion in the Nepal high Himalaya. *Geomorphology*, 97(1-2), 5–23. Available from: https://doi.org/10.1016/j.geomorph.2007.02.046

Holzhauser, H., Magny, M. & Zumbühl, H.J. (2005) Glacier and lake-level variations in west-central Europe over the last 3500 years. *The Holocene*, 15(6), 789–801. Available from: https://doi.org/10.1191/0959683605hl853ra

Huggel, C., Allen, S., Deline, P., Fischer, L., Noetzli, J. & Ravanel, L. (2012) Ice thawing, mountains falling - are alpine rock slope failures increasing? *Geology Today*, 28(3), 98–104. Available from: https://doi.org/10.1111/j.1365-2451.2012.00836.x

Huggel, C., Salzmann, N., Allen, S., Caplan-Auerbach, J., Fischer, L., Haeberli, W., Larsen, C., Schneider, D. & Wessels, R. (2010) Recent and future warm extreme events and high-mountain slope stability. *Philosophical Transactions of the Royal Society A*, 368(1919), 2435–2459. Available from: https://doi.org/10.1098/rsta.2010.0078

Huss, M. (2012) Extrapolating glacier mass balance to the mountain-range scale: the European Alps 1900-2100. *The Cryosphere*, 6(4), 713–727. Available from: https://doi.org/10.5194/tc-6-713-2012

Ivy-Ochs, S., Kerschner, H., Maisch, M., Christl, M., Kubik, P.W. & Schlüchter, C. (2009) Latest Pleistocene and Holocene glacier variations in the European Alps. *Quaternary Science Reviews*, 28(21–22), 2137–2149. Available from: https://doi.org/10.1016/j.quascirev.2009.03.009

Kirkbride, M.P. (1993) The temporal significance of transitions from melting to calving termini at glaciers in the central Southern Alps of New Zealand. *Holocene*, 3(3), 232–240. Available from: https://doi.org/10.1177/095968369300300305

Kirkbride, M.P. (1995) Processes of transportation. In: Menzies, J. (Ed.) *Modern glacial environments: processes, dynamics and sediments*, Vol. 1. Butterworth-Heinemann: Oxford, pp. 261–292.

Kober, F., Hippe, K., Salcher, B., Ivy-Ochs, S., Kubik, P.W., Wacker, L. & Hählen, N. (2012) Debris-flow-dependent variation of cosmogenically derived catchment-wide denudation rates. *Geology*, 40(10), 935–938. Available from: https://doi.org/10.1130/G33406.1

Korschinek, G., Bergmaier, A., Faestermann, T., Gerstmann, U.C., Knie, K., Rugel, G., Wallner, A., Dillmann, I., Dollinger, G., Lierse von Gostomski, Ch. Kossert, K., Maiti, M., Poutivtsev, M. & Remmert, A. (2010) A new value for the half-life of ^{10}Be by Heavy-Ion Elastic Recoil Detection and liquid scintillation counting. *Nuclear Instruments and Methods in Physics Research B: Beam Interactions with Materials and Atoms*, 268(2), 187–191. Available from: https://doi.org/10.1016/j.nimb.2009.09.020

Kurowski, L. (1891) Die Höhe der Schneegrenze mit besonderer Berücksichtigung der Finsteraarhorn-Gruppe. *Penck'S Geographische Abhandlungen*, 5, 119–160.

Lal, D. (1991) Cosmic ray labeling of erosion surfaces: in situ nuclide production rates and erosion models. *Earth and Planetary Science Letters*, 104(2-4), 424–439. Available from: https://doi.org/10.1016/0012-821X(91)90220-C

Lambiel, C. & Talon, P. (2019) Les glaciers du haut val de Bagnes au Petit Age glaciaire. Annales valaisannes. *Actes du colloque Giétro 1818 sous la loupe des sciences*, 63–75.

Langhammer, L., Rabenstein, L., Bauder, A. & Maurer, H. (2017) Ground-penetrating radar antenna orientation effects on temperate mountain glaciers. *Geophysics*, 82(3), H15–H24. Available from: https://doi.org/10.1190/geo2016-0341.1

Lehmann, B., Herman, F., Valla, P.G., King, G.E., Biswas, R.H., Ivy-Ochs, S., Steinemann, O. & Christl, M. (2020) Postglacial erosion of bedrock surfaces and deglaciation timing: New insights from the Mont Blanc massif (western Alps). *Geology*, 48(2), 139–144. Available from: https://doi.org/10.1130/G46585.1

Leprince, S., Barbot, S., Ayoub, F. & Avouac, J.-P. (2007) Automatic and precise orthorectification, coregistration, and subpixel correlation of satellite images, application to ground deformation measurements. *IEEE Transactions on Geoscience and Remote Sensing*, 45(6), 1529–1558. Available from: https://doi.org/10.1109/TGRS.2006.888937

Lukens, C.E., Riebe, C.S., Sklar, L.S. & Shuster, D.L. (2016) Grain size bias in cosmogenic nuclide studies of stream sediment in steep terrain. *Journal of Geophysical Research - Earth Surface*, 121(5), 978–999. Available from: https://doi.org/10.1002/2016JF003859

Mair, D., Lechmann, A., Delunel, R., Yeşilyurt, S., Tikhomirov, D., Vockenhuber, C., Christl, M., Akçar, N. & Schlunegger, F. (2020) The role of frost cracking in local denudation of steep Alpine rockwalls over millennia (Eiger, Switzerland). *Earth Surface Dynamics*, 8(3), 637–659. Available from: https://doi.org/10.5194/esurf-8-637-2020

Mair, D., Lechmann, A., Yeşilyurt, S., Tikhomirov, D., Delunel, R., Vockenhuber, C., Akçar, N. & Schlunegger, F. (2019) Fast long-term denudation rate of steep alpine headwalls inferred from cosmogenic ^{36}Cl depth profiles. *Scientific Reports*, 9(1), 1–15. Available from: https://doi.org/10.1038/s41598-019-46969-0

Maisch, M., Wipf, A., Denneler, B., Battaglia, J. & Benz, C. (2000) Die Gletscher der Schweizer Alpen: Gletscherhochstand 1850, Aktuelle Vergletscherung, Gletscherschwund-Szenarien. (Schlussbericht NFP 31). 2. Auflage. vdf Hochschulverlag an der ETH Zürich, 373 pp. & Paul, F. 2004, The new Swiss glacier inventory 2000 - application of remote sensing and GIS. PhD Thesis, Department of Geography, University of Zurich, *Schriftenreihe Physische Geographie*, **52**, 210 pp.

Mancini, D. & Lane, S.N. (2020) Changes in sediment connectivity following glacial debuttressing in an Alpine valley system. *Geomorphology*, 352, 106987. Available from: https://doi.org/10.1016/j.geomorph.2019.106987

Masarik, J., Kollar, D. & Vanya, S. (2000) Numerical simulation of in situ production of cosmogenic nuclides: Effects of irradiation geometry. *Nuclear Instruments and Methods in Physics Research Section B: Beam Interactions with Materials and Atoms*, 172(1–4), 786–789. Available from: https://doi.org/10.1016/S0168-583X(00)00121-X

Matmon, A., Bierman, P.R., Larsen, J., Southworth, S., Pavich, M., Finkel, R. & Caffee, M. (2003) Erosion of an ancient mountain range, the Great Smoky Mountains, North Carolina and Tennessee. *American Journal of Science*, 303(9), 817–855. Available from: https://doi.org/10.2475/ajs.303.9.817

Mattson, L. E., Gardner, J. S. & Young, G. J. (1993) Ablation on debris covered glaciers: an example from the Rakhiot Glacier, Punjab, Himalaya, *IAHS Publication*, **218** (Symposium at Kathmandu, Nepal 1992 - *Snow and Glacier Hydrology*), 289–296.

Müller, F., Caflisch, T. & Müller, G. (1976) Firn und Eis der Schweizer Alpen (Gletscherinventar). Publ. Nr. 57/57a. Geographisches Institut, ETH Zürich, 2 Vols. & Maisch, M., Wipf, A., Denneler, B., Battaglia, J. & Benz, C. 2000, Die Gletscher der Schweizer Alpen: Gletscherhochstand 1850, Aktuelle Vergletscherung, Gletscher schwund-Szenarien. (Schlussbericht NFP 31). 2. Auflage. vdf Hochschulverlag an der ETH Zürich, 373 pp. & Paul, F. 2004, The new Swiss glacier inventory 2000 - application of remote sensing and GIS. PhD Thesis, Department of Geography, University of Zurich, *Schriftenreihe Physische Geographie*, **52**, 210 pp.

NASA Shuttle Radar Topography Mission SRTM. (2013) Shuttle Radar Topography Mission (SRTM) Global. Distributed by OpenTopography. Available from: https://doi.org/10.5069/G9445JDF. (Accessed: 21/05/2021).

Nicholson, L. & Benn, D.I. (2006) Calculating ice melt beneath a debris layer using meteorological data. *Journal of Glaciology*, 52(178), 463–470. Available from: https://doi.org/10.3189/172756506781828584

Niemi, N.A., Oskin, M., Burbank, D.W., Heimsath, A.M. & Gabet, E.J. (2005) Effects of bedrock landslides on cosmogenically determined erosion rates. *Earth and Planetary Science Letters*, 237(3–4), 480–498. Available from: https://doi.org/10.1016/j.epsl.2005.07.009

Østrem, G. (1959) Ice melting under a thin layer of moraine, and the existence of ice cores in moraine ridges. *Geografiska Annaler*, 41(4), 228–230. Available from: https://doi.org/10.1080/20014422.1959.11907953

Paul, F., Kääb, A., Maisch, M., Kellenberger, T. & Haeberli, W. (2004) Rapid disintegration of Alpine glaciers observed with satellite data. *Geophysical Research Letters*, 31(21), L21402. Available from: https://doi.org/10.1029/2004GL020816

Phillips, M., Wolter, A., Lüthi, R., Amann, F., Kenner, R. & Bühler, Y. (2016) Rock slope failure in a recently deglaciated permafrost rock wall at Piz Kesch (Eastern Swiss Alps), February 2014. *Earth Surface Processes and Landforms*, 42(3), 426–438. Available from: https://doi.org/10.1002/esp.3992

Puchol, N., Lavé, J., Lupker, M., Blard, P.-H., Gallo, F. & France-Lanord, C. (2014) Grain size dependent concentration of cosmogenic ^{10}Be and erosion dynamics in a landslide-dominated Himalayan watershed. *Geomorphology*, 224, 55–68. Available from: https://doi.org/10.1016/j.geomorph.2014.06.019

Rabatel, A., Deline, P., Jaillet, S. & Ravanel, L. (2008) Rock falls in high-alpine rock walls quantified by terrestrial lidar measurements: A case study in the Mont Blanc area. *Geophysical Research Letters*, 35(10), L10502. Available from: https://doi.org/10.1029/2008GL033424

Ravanel, L., Allignol, F., Deline, P., Gruber, S. & Ravello, M. (2010) Rock falls in the Mont Blanc Massif in 2007 and 2008. *Landslides*, 7(4), 493–501. Available from: https://doi.org/10.1007/s10346-010-0206-z

Ravanel, L. & Deline, P. (2009) La face ouest des Drus (massif du Mont-Blanc): évolution de l'instabilité d'une paroi rocheuse dans la haute

montagne alpine depuis la fin du petit âge glaciaire. *Géomorphologie: Relief, Processus, Environnement*, 4(4), 261–272. Available from: https://doi.org/10.4000/geomorphologie.7444

Ravanel, L. & Deline, P. (2011) Climate influence on rockfalls in high-Alpine steep rockwalls: The north side of the Aiguilles de Chamonix (Mont Blanc massif) since the end of the 'Little Ice Age.'. *The Holocene*, 21, 357–365. Available from: https://doi.org/10.1177/0959683610374887

Ravanel, L., Magnin, F. & Deline, P. (2017) Impacts of the 2003 and 2015 summer heatwaves on permafrost-affected rock-walls in the Mont Blanc massif. *Science of the Total Environment*, 609, 132–143. Available from: https://doi.org/10.1016/j.scitotenv.2017.07.055

Reid, T.D. & Brock, B.W. (2010) An energy-balance model for debris-covered glaciers including heat conduction through the debris layer. *Journal of Glaciology*, 56(199), 903–916. Available from: https://doi.org/10.3189/002214310794457218

Rempel, A.W., Marshall, J.A. & Roering, J.J. (2016) Modeling relative frost weathering rates at geomorphic scales. *Earth and Planetary Science Letters*, 453, 87–95. Available from: https://doi.org/10.1016/j.epsl.2016.08.019

Rowan, A.V., Egholm, D.L., Quincey, D.J. & Glasser, N.F. (2015) Modelling the feedbacks between mass balance, ice flow and debris transport to predict the response to climate change of debris-covered glaciers in the Himalaya. *Earth and Planetary Science Letters*, 430, 427–438. Available from: https://doi.org/10.1016/j.epsl.2015.09.004

Ruiz-Carulla, R., Corominas, J. & Mavrouli, O. (2015) A methodology to obtain the block size distribution of fragmental rockfall deposits. *Landslides*, 12(4), 815–825. Available from: https://doi.org/10.1007/s10346-015-0600-7

Ruiz-Carulla, R., Corominas, J. & Mavrouli, O. (2017) A fractal fragmentation model for rockfalls. *Landslides*, 14(3), 875–889. Available from: https://doi.org/10.1007/s10346-016-0773-8

Sarr, A.-C., Mugnier, J.-L., Abrahami, R., Carcaillet, J. & Ravanel, L. (2019) Sidewall erosion: Insights from in situ-produced ^{10}Be concentrations measured on supraglacial clasts (Mont Blanc massif, France). *Earth Surface Processes and Landforms*, 44(10), 1930–1944. Available from: https://doi.org/10.1002/esp.4620

Sass, O. (2005) Spatial patterns of rockfall intensity in the northern Alps. *Zeitschrift für Geomorphologie Supplementband*, 138, 51–65.

Sass, O. (2007) Bedrock detection and talus thickness assessment in the European Alps using geophysical methods. *Journal of Applied Geophysics*, 62(3), 254–269. Available from: https://doi.org/10.1016/j.jappgeo.2006.12.003

Sass, O. (2010) Spatial and temporal patterns of talus activity - a lichenometric approach in the Stubaier Alps, Austria. *Geografiska Annaler. Series A, Physical Geography*, 92(3), 375–391. Available from: https://doi.org/10.1111/j.1468-0459.2010.00402.x

Scherler, D., Bookhagen, B. & Strecker, M.R. (2011) Spatially variable response of Himalayan glaciers to climate change affected by debris cover. *Nature Geoscience*, 4(3), 156–159. Available from: https://doi.org/10.1038/NGEO1068

Scherler, D. & Egholm, D.L. (2020) Production and transport of supraglacial debris: Insights from cosmogenic ^{10}Be and numerical modeling, Chhota Shigri Glacier, Indian Himalaya. *Journal of Geophysical Research - Earth Surface*, 125(10), e2020JF005586. Available from: https://doi.org/10.1029/2020JF005586

Scherler, D., Leprince, S. & Strecker, M.R. (2008) Glacier-surface velocities in alpine terrain from optical satellite imagery - Accuracy improvement and quality assessment. *Remote Sensing of Environment*, 112(10), 3806–3819. Available from: https://doi.org/10.1016/j.rse.2008.05.018

Schwanghart, W. & Scherler, D. (2014) Short Communication: TopoToolbox 2 - MATLAB-based software for topographic analysis and modeling in Earth surface sciences. *Earth Surface Dynamics*, 2(1), 1–7. Available from: https://doi.org/10.5194/esurf-2-1-2014

Seong, Y.B., Owen, L.A., Caffee, M.W., Kamp, U., Bishop, M.P., Bush, A., Copland, L. & Shroder, J.F. (2009) Rates of basin-wide rockwall retreat in the K2 region of the Central Karakoram defined by terrestrial cosmogenic nuclide ^{10}Be. *Geomorphology*, 107(3-4), 254–262. Available from: https://doi.org/10.1016/j.geomorph.2008.12.014

Stone, J.O. (2000) Air pressure and cosmogenic isotope production. *Journal of Geophysical Research*, 105(B10), 23753–23759. Available from: https://doi.org/10.1029/2000JB900181

Swisstopo. (2021) [homepage on the internet]. Federal Office of Topography swisstopo. Available from: https://map.geo.admin.ch. (Accessed: 21/05/2021).

Tofelde, S., Duesing, W., Schildgen, T.F., Wickert, A.D., Wittmann, H., Alonso, R.N. & Strecker, M. (2018) Effects of deep-seated versus shallow hillslope processes on cosmogenic ^{10}Be concentrations in fluvial sand and gravel. *Earth Surface Processes and Landforms*, 43(15), 3086–3098. Available from: https://doi.org/10.1002/esp.4471

van Dongen, R., Scherler, D., Wittmann, H. & von Blanckenburg, F. (2019) Cosmogenic ^{10}Be in river sediment: where grain size matters and why. *Earth Surface Dynamics*, 7(2), 393–410. Available from: https://doi.org/10.5194/esurf-7-393-2019

Vincent, C., Wagnon, P., Shea, J.M., Immerzeel, W.W., Kraaijenbrink, P., Shrestha, D., Soruco, A., Arnaud, Y., Brun, F., Berthier, E. & Sherpa, S.F. (2016) Reduced melt on debris-covered glaciers: investigations from Changri Nup Glacier, Nepal. *The Cryosphere*, 10(4), 1845–1858. Available from: https://doi.org/10.5194/tc-10-1845-2016

von Blanckenburg, F., Hewawasam, T. & Kubik, P.W. (2004) Cosmogenic nuclide evidence for low weathering and denudation in the wet, tropical highlands of Sri Lanka. *Journal of Geophysical Research*, 109(F3), F03008. Available from: https://doi.org/10.1029/2003JF000049

Ward, D.J. & Anderson, R.S. (2011) The use of ablation-dominated medial moraines as samplers for ^{10}Be-derived erosion rates of glacier valley walls, Kichatna Mountains, AK. *Earth Surface Processes and Landforms*, 36(4), 495–512. Available from: https://doi.org/10.1002/esp.2068

West, A.J., Hetzel, R., Li, G., Jin, Z., Zhang, F., Hilton, R.G. & Densmore, A.L. (2014) Dilution of ^{10}Be in detrital quartz by earthquake-induced landslides: Implications for determining denudation rates and potential to provide insights into landslide sediment dynamics. *Earth and Planetary Science Letters*, 396, 143–153. Available from: https://doi.org/10.1016/j.epsl.2014.03.058

Wetterauer, K., Scherler, D., Anderson, L.S. & Wittmann, H. (2022) *Sample and Modelling Data for Cosmogenic 10Be in Medial Moraine Debris of Glacier d'Otemma, Switzerland*. GFZ Data Services. Available from: https://doi.org/10.5880/GFZ.3.3.2021.007

Wittmann, H., von Blanckenburg, F., Kruesmann, T., Norton, K.P. & Kubik, P.W. (2007) Relation between rock uplift and denudation from cosmogenic nuclides in river sediment in the Central Alps of Switzerland. *Journal of Geophysical Research - Earth Surface*, 112(F4), F04010. Available from: https://doi.org/10.1029/2006JF000729

Zemp, M., Huss, M., Thibert, E., Eckert, N., McNabb, R., Huber, J., Barandun, M., Machguth, H., Nussbaumer, S.U., Gärtner-Roer, I., Thomson, L., Paul, F., Maussion, F., Kutuzov, S. & Cogley, J.G. (2019) Global glacier mass changes and their contributions to sea-level rise from 1961 to 2016. *Nature*, 568(7752), 382–386. Available from: https://doi.org/10.1038/s41586-019-1071-0

Zemp, M., Paul, F., Hoelzle, M. & Haeberli, W. (2008) Glacier fluctuations in the European Alps, 1850–2000: an overview and spatio-temporal analysis of available data. In: Orlove, B., Wiegandt, E. & Luckman, B.H. (Eds.) *Darkening Peaks: Glacier Retreat, Science, and Society*. Berkeley, US: University of California Press, pp. 152–167. Available from: https://doi.org/10.5167/uzh-9024

How to cite this article: Wetterauer, K., Scherler, D., Anderson, L.S. & Wittmann, H. (2022) Temporal evolution of headwall erosion rates derived from cosmogenic nuclide concentrations in the medial moraines of Glacier d'Otemma, Switzerland. *Earth Surface Processes and Landforms*, 47(10), 2437–2454. Available from: https://doi.org/10.1002/esp.5386